Received: 16 July 2021 | Revised: 23 August 2021 | Accepted: 8 September 2021

DOI: 10.1002/cta.3147

COMPREHENSIVE REVIEW

WILEY

Nonlinear models of power inductors: A survey

Alberto Oliveri | **Matteo Lodi** | **Marco Storace**

Department of Electrical, Electronic, Telecommunications Engineering and Naval Architecture, University of Genoa, Genova, Italy

Correspondence
Marco Storace, University of Genoa, Via Opera Pia 11A, Genova 16145, Italy.
Email: marco.storace@unige.it

Summary

Switch-mode power supplies (SMPSs) are widely exploited to interface electrical energy sources to motors and other electrical loads. Inductors are usually the biggest and heaviest components in SMPSs, limiting their overall power density. Therefore, there is an increasing interest in designing SMPSs with partially saturating inductors, because this significantly reduces their weight and size, thus increasing power density. This paper provides a review of nonlinear behavioral models (based on easy-to-measure quantities) of the inductance, power loss, and temperature rise of inductors working, at least partially, in magnetic saturation. This survey discusses the pros, cons, and ranges of validity of these models, with a glimpse at their application to SMPS simulation, design, monitoring, and control.

KEYWORDS

inductance, nonlinear models, power inductors, saturation, switch-mode power supplies

1 | INTRODUCTION

The European Green Deal[1] aims at achieving a reduction of greenhouse gases emission in 2030 of at least 50%, compared to 1990, and reaching zero net emissions by 2050. Transportation accounts for a quarter of the EU's greenhouse gas emissions, and it is estimated that to pursue the EU's targets, a 90% reduction in transport emissions (road, rail, aviation, and waterborne) is needed by 2050. Therefore, electrification of transport is a priority. In the last decade, the availability on the market of mild-hybrid,[2] full-hybrid, plug-in hybrid, and full-electric cars has grown exponentially,[3] from small city-cars to big sport utility vehicles (SUVs). In *more electric aircrafts*, the hydraulic and pneumatic systems are replaced by electric devices[4] and the research is moving towards all-electric airplanes, where also the propulsion system becomes electrical.[5]

In this context, switch-mode power supplies (SMPSs) interfacing batteries, motors, and other electrical loads are widely exploited.[6] SMPSs convert input power at a given voltage and current level to output power at a different voltage and current level, by storing energy in capacitors and inductors, converting that energy into packets using semiconductor switches, and then releasing packets to the output. Achieving a high power density (defined as the ratio between power and volume) is of paramount importance in the automotive and aerospace fields since smaller and therefore lighter converters contribute to lowering the overall vehicle power consumption,[4,5,7-9] and size can be an issue especially in small vehicles. The reduction of inductor size is crucial also in other contexts, for example, for electromagnetic interference filters[10] or magnetic energy harvesters.[11]

Inductors are usually the biggest and heaviest components in SMPSs,[12] limiting the overall power density. As well known, a current flowing through the inductor wire induces a magnetic flux across the windings. For sufficiently low

currents, the flux can be assumed to be proportional to the current through a constant coefficient (the inductance),[13] which is the main parameter describing the inductor. However, over a certain current threshold, magnetic core saturation occurs, causing the flux to increase much more slowly. In other words, the inductance decreases as the current increases. Reducing the core size without modifying the inductance requires adding more windings, which in turn implies that the core starts saturating at lower current values.

Saturation is traditionally avoided in the SMPS design because a decrease of the inductance implies an increase of the current ripple and, therefore, of temperature and power loss. Moreover, the classical linear inductor model, where the inductance is constant, can no longer be applied, making the SMPS design and simulation much more involved. However, in 2012, Milner and Rincón-Mora[14] verified experimentally that SMPSs can exploit smaller saturating inductors, with a limited loss in efficiency. In particular, they verified that a 3.3 × 3.3 × 1.0 mm 3 ferrite-core inductor with a nominal inductance of 1 H and rated for a 1.6-A current (Coilcraft LPO3310) can properly work in saturation with a current up to 2.1 A. Compared to the smallest nonsaturating inductor with a rated current of 2.1 A, the LPO3310 allows achieving a 50% area reduction, a 65% volume reduction with only a 2.7% increase of the peak power loss. Concerns about the use of saturating inductors are successively demystified by several works by Femia et al,[15-19] showing through theory and experiments that saturation is not always a *problem*, but it is rather a *solution* if it is properly modeled and the SMPS is designed accounting for its effects.

Inductor saturation and power loss can be modeled by resorting to physics-based electromagnetic models,[20-24] which are accurate but unpractical, since they require the knowledge of geometrical and physical properties of the inductor, not always disclosed for commercial devices, and involve electric and magnetic fields. The work by Milner and Rincón-Mora motivated the development of behavioral inductor models able to estimate the inductance, power loss, and temperature rise based on easy-to-measure electrical variables. Tens of models have been developed in the last decade, with their own pros and cons and ranges of validity. A previous survey[25] focuses on about 10 behavioral inductance models. This paper provides a much wider description and critical discussion of inductance, power loss, and temperature behavioral models, showing how they are exploited for SMPS simulation, design, monitoring, and control.

The increasing interest in this topic is witnessed by two other recent surveys by Di Capua et al[18] and Kaiser and Duerbaum.[26] The former discusses the effects of inductor saturation on the SMPS operation, whereas the latter presents a review on the application of power supplies with saturating inductors in the automotive, aerospace, battery charging, lighting, and photovoltaic fields, by pointing out the reasons why saturation is exploited.

This survey is organized as follows. The general concepts about nonlinear power inductors and buck/boost converters are summarized in Sections 2.1 and 3, respectively. Sections 4 and 5 list the main behavioral inductance and power loss models suitable for saturating inductors, whereas Section 6 is focused on the application of these models for SMPS simulation, design, monitoring, and control. Finally, some conclusions are drawn in Section 7.

2 | BASIC CONCEPTS

Inductors are passive two-terminal electrical components realized by winding a conductive wire around a core (Figure 1A). According to the Ampère–Maxwell law, when a current i flows through the wire, fields H (magnetic field

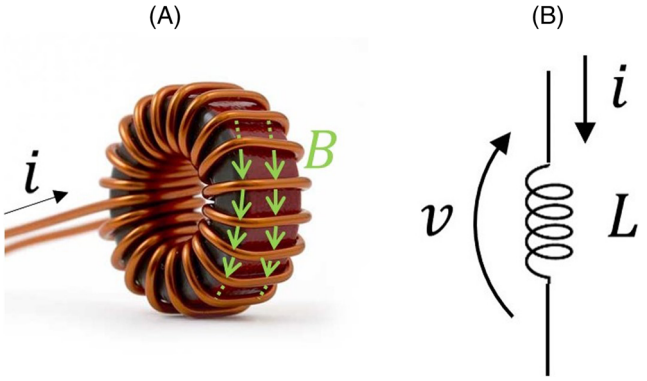

FIGURE 1 Example of toroidal inductor (A) and its circuit symbol (B) [Colour figure can be viewed at wileyonlinelibrary.com]

strength, measured in [A m^{-1}]) and B (magnetic flux density, measured in [T]) are generated within the core. Let Φ be the flux of field B across the windings. According to the Maxwell–Faraday equation, a time variation of this flux induces an electromotive force which tends to generate a current opposite to the impressed one i, in order to contrast the flux variation (Lenz's law). This results in a voltage across the inductor terminals

$$v = \frac{d\Phi}{dt}, \tag{1}$$

with the reference directions shown in Figure 1B. In the following, we will denote as H and B the magnitude of the fields, without considering their direction, as the fields are aligned in the common case of isotropic materials.

The relationship between fields B and H depends on the core material. For paramagnetic materials (e.g., air), B is proportional to H through a scalar (in case of isotropic material) coefficient μ referred to as *magnetic permeability*,

$$B = \mu H. \tag{2}$$

Permeability can be expressed as $\mu = \mu_r \mu_0$, where $\mu_0 = 4\pi \cdot 10^{-7}$ H m^{-1} is the permeability of the vacuum, whereas μ_r (dimensionless) is the relative permeability, which for paramagnetic materials is slightly larger than 1. In ferromagnetic materials (e.g., ferrite), for a given field H, the induced field B is orders of magnitude higher than for paramagnetic materials, but the relationship between the two fields is strongly nonlinear (Figure 2), exhibiting a temperature-dependent hysteresis loop which is traveled counterclockwise. The shape of the loop depends on the considered material and its fabrication process.

If a (say positive) field H is applied to the material and then brought back to zero, the field B does not return to zero, meaning that the material has been magnetized. A negative field H must be applied again to demagnetize the material. The strength of the demagnetization field is referred to as *coercitivity*. For the design of a permanent magnet, it is desirable to have a wide hysteresis loop (high coercitivity). By contrast, for inductor cores, the hysteresis represents an undesired nonlinear effect, which also increases the power loss (see Section 5), being the area of the hysteresis loop proportional to the dissipated energy. Therefore, *soft* (i.e., with low coercitivity) magnetic cores are usually exploited, which are characterized by a narrow hysteresis loop. Examples of soft materials are ferrite, iron powder, amorphous, or nanocrystalline alloys.

Another relevant effect that can be noticed by looking at Figure 2 is saturation: if the field H is increased (decreased) above a certain value, the field B increases (decreases) very slowly, as for paramagnetic materials. This behavior can be noticed also in the *first magnetization curve* (Figure 3A), which is obtained starting from zero fields and by increasing the H field. In this case, the relative permeability μ_r is a function of the field H, as shown in Figure 3B.

The differential permeability,

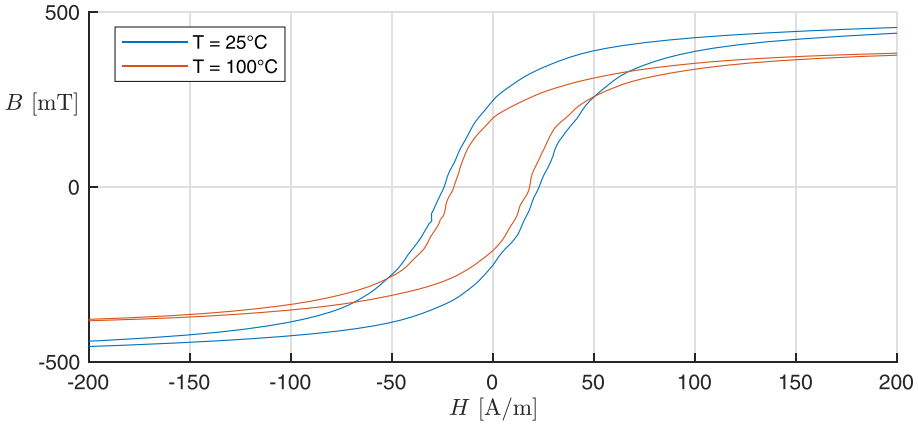

FIGURE 2 Relationship between B and H in the N27 ferrite material, provided by TDK Electronics Design Tool[27] at 25°C (blue line) and 100°C (red line) [Colour figure can be viewed at wileyonlinelibrary.com]

$$\mu_d(H) = \frac{dB}{dH}, \tag{3}$$

is shown in Figure 3C. For ferrites, the differential permeability quickly decreases as H overcomes a threshold. Other materials, for example, made of iron powder, exhibit a smoother decrease of μ_d.

The permeability μ strongly depends also on the core temperature T. For example, for ferrite cores, as the temperature increases, the core starts saturating at lower values of H. Therefore, both relative and differential permeability start dropping at lower values of H. Notice that for low values of H, where the slope μ_d of the magnetization curve is almost constant, the ferromagnetic material approximately behaves like a linear medium and the temperature dependence is negligible.

Finally, in the case of sinusoidal field H, the permeability is a complex function of its frequency. At low rates, there is an algebraic relationship between H and B. When the frequency increases above a certain threshold (which depends on the material), B is no longer able to follow H instantaneously. This induces a phase shift between H and B, which causes an enlargement of the hysteresis loop and an increase in the power loss. Figure 4 shows the real part of μ_r versus the excitation frequency for a ferrite material. It is evident that, at frequencies above 1 MHz, the permeability drastically drops.

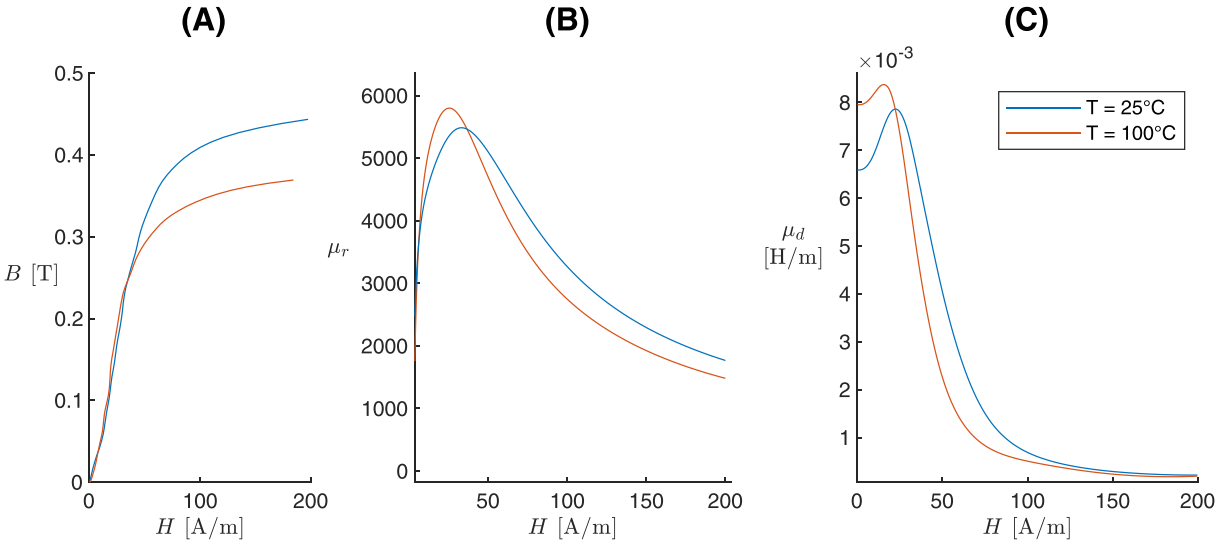

FIGURE 3 First magnetization curve (A), relative permeability (B), and differential permeability (C) of the N27 ferrite material at 25°C (blue lines) and 100°C (red lines). Data are obtained from the TDK Electronics Design Tool[27] [Colour figure can be viewed at wileyonlinelibrary.com]

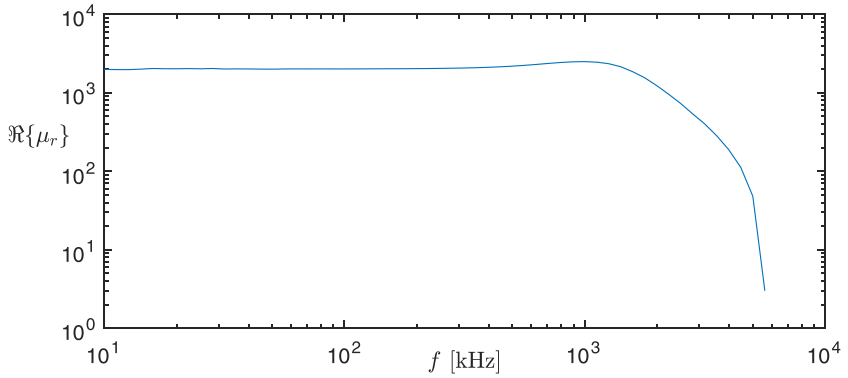

FIGURE 4 Relationship between the real part of μ_r and the frequency f for the N27 ferrite material, provided by TDK Electronics Design Tool[27] [Colour figure can be viewed at wileyonlinelibrary.com]

When a wire is wounded around a magnetic core, an inductor is created, where the field H is proportional to the inductor current, whereas the magnetic flux is proportional to the field B. Therefore, the relationship between B and H corresponds to an analogous relationship between flux Φ and current i. Figure 5, for instance, shows the relationship between Φ and i, measured on a Coilcraft DO3316T-103 ferrite-core inductor at different core temperatures $T_2 > T_1$. Notice the similarity with the B-H curves shown in Figure 3A, where the slope of the curve is initially high and decreases as H increases. By applying Equation (1), we obtain

$$v = \frac{d\Phi}{dt} = \frac{d\Phi}{di}\frac{di}{dt} = L(i)\frac{di}{dt}, \tag{4}$$

where $L(i)$ is the differential inductance (simply referred to as inductance in the remainder of the paper), which is related to the differential permeability μ_d, as illustrated in the following example. Let us consider a cylindrical inductor with n turns, length l and radius r, with $l \gg r$. In this case, it is easy to obtain that $H = \frac{n}{l}i$ (Ampère–Maxwell law) and $\Phi = Bn\pi r^2$. Therefore,

$$L(i) = \frac{d\Phi}{di} = \frac{n\pi r^2 dB}{\frac{l}{n}dH} = \frac{n^2\pi r^2}{l}\frac{dB}{dH} = \frac{n^2\pi r^2}{l}\mu_d(H). \tag{5}$$

In other words, $L(i)$ is proportional to the differential permeability of the core material, through some geometric properties of the inductor. Being related to the permeability, the inductance $L(i)$ turns out to be qualitatively similar to the function shown in Figure 3C and depends also on the core temperature and the working frequency. Moreover, the

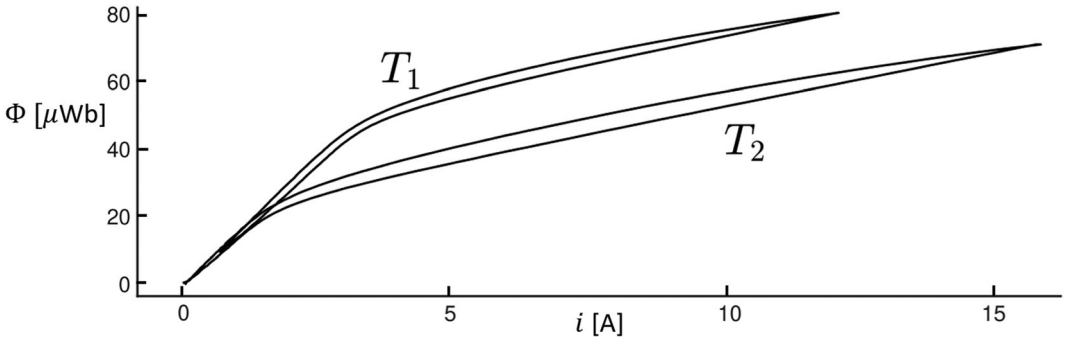

FIGURE 5 Φ versus i hysteretic curves measured on a Coilcraft DO3316T-103 ferrite-core inductor at different core temperatures $T_2 > T_1$

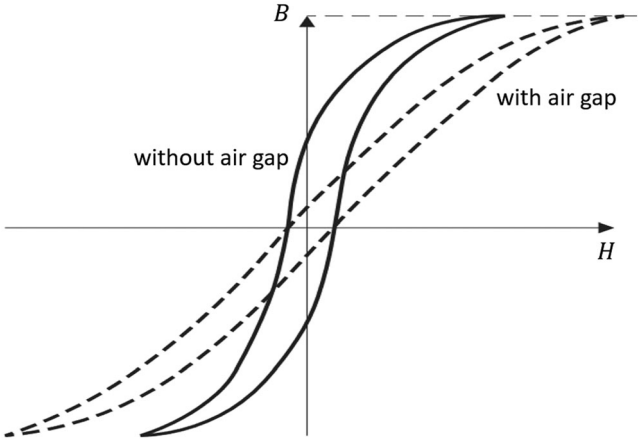

FIGURE 6 Relationship between B and H in a ferrite core[28] with (dashed curve) and without (solid curve) air gap

inductance can be assumed to have a constant value L_{nom} (nominal inductance) only if the current remains below a given threshold (depending on temperature). By looking at Equation (5), it appears that L_{nom} is proportional to the square of the number of turns. Moreover, for a fixed value of i, an inductor with a higher number of turns will generate stronger fields H and then B, meaning that the core will saturate at lower current values. Therefore, for a given core, an inductor with a higher number of turns has a higher nominal inductance but starts saturating at lower current values. The value of the current where saturation begins also depends on the permeability of the material. The higher the permeability, the lower the field H (and therefore the current) leading to the saturation of B. Usually, in commercial ferrite-core inductors, an air gap is inserted in the core, to decrease the overall permeability, thus allowing the inductor to operate in its linear region for a wider current range. Figure 6 shows the relationship between B and H in a ferrite core[28] with (dashed curve) and without (solid curve) air gap.

2.1 | Power inductors

Inductors are used for several applications, in particular, radio frequency systems, power electronics, electromagnetic interference filtering, and transformers. The focus of this survey is on power inductors, which are usually characterized by soft ferromagnetic cores, as they need to store a large amount of energy with power loss as low as possible. Consider two inductors (A and B) with the same core material, characterized by its magnetization curve. Inductor A has a larger core size (i.e., radius r) and a lower number of windings n compared to inductor B, but the inductance of the two components is the same. This is possible since, from Equation (5), it appears that L is proportional to both r^2 and n^2. For the same value of i, inductor B (smaller) generates a higher field H (proportional to n), which implies that the core of inductor B will saturate for lower current values. Therefore, for a bigger core, we can assume with acceptable accuracy that $L = L_{nom}$ for a wider range of current. This is the reason why power converter manufacturers tend to use bulky inductors.

Power inductors are key components in SMPSs, as they mainly determine the current ripple and power loss. In order to exploit smaller inductors working in partial saturation, accurate models of the inductance and power loss are necessary to design, simulate, monitor, and control power converters. The characterization of the material in terms of magnetization curve, provided by some manufacturers,[29] is not practical to this aim because fields H and B are not easily measurable on circuits and the relationship between these fields and the inductor voltage and current depends on several geometric properties of the inductor, which are often not provided, at least for commercial inductors. The manufacturers' datasheets do not always provide a full inductor characterization in the saturation region (as it is traditionally avoided in the inductor functioning), and whenever it is provided, it is usually obtained by applying to the inductor small-amplitude sinusoidal signals, which are very different from the signals that are applied to the inductor (e.g., square waves). These nonsinusoidal signals contain several harmonics, which may affect the permeability, as discussed above. All these aspects motivated the need to develop accurate inductor models, based on easy-to-measure quantities, providing a reliable estimate of both the inductance and the power loss. SMPSs are assumed to work in a limited range of frequencies; therefore, the dependence of the permeability on the field rate is not taken into account. These models are usually identified by applying to the inductor realistic voltage profiles and can be exploited in circuit simulators. The models can be possibly embedded in digital circuits (microcontrollers or FPGAs) for SMPS online monitoring and control.

3 | SWITCH MODE POWER SUPPLIES

Power inductors are commonly employed in transformers (as coupled inductors), chokes, filters, and power converters, in particular SMPSs. The simplest topologies, used to identify and validate the majority of the nonlinear inductor models, are the buck and boost converter, whose circuit diagrams are shown in Figure 7, panels (A) and (B), respectively.

The buck (boost) converter converts a DC input voltage v_{in} into a lower (higher) DC output voltage v_{out}. Both architectures exploit an inductor with voltage v and current i, an output capacitor, one diode with voltage drop v_d, and an MOS transistor operating as a switch, usually driven by a pulse-width modulation (PWM) signal with frequency f and duty cycle d. The output current is i_{out}, whereas R_L and R_{mos} denote the inductor parasitic resistance (representing the DC winding loss, described in Section 5.1) and the MOS resistance during the ON state, respectively.

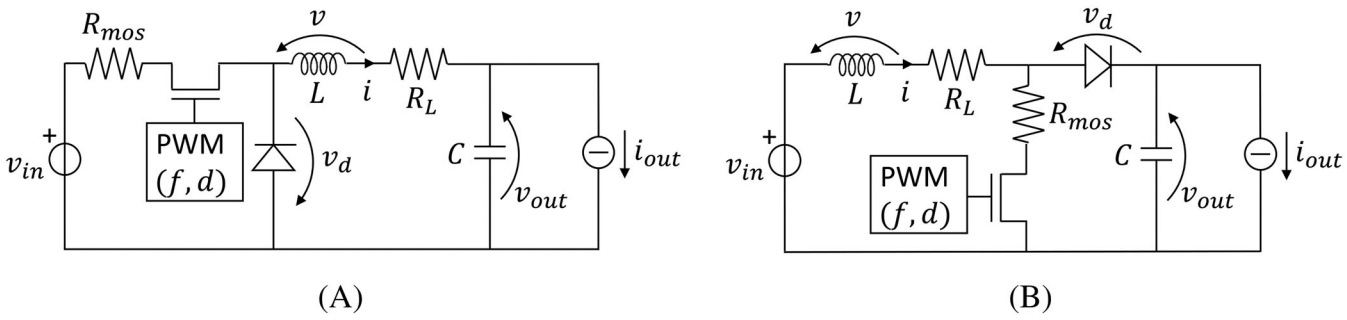

FIGURE 7 Circuit diagram of a buck (A) and boost (B) DC-DC converter

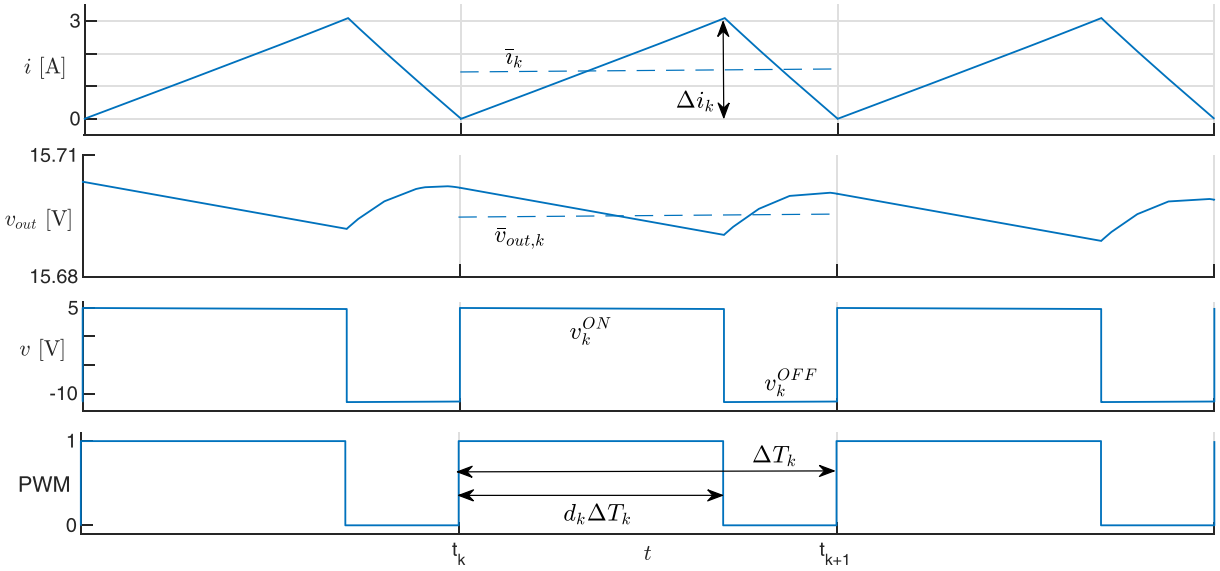

FIGURE 8 Typical steady-state waveforms of i, v_{out}, v, and PWM signal, from top to bottom, respectively [Colour figure can be viewed at wileyonlinelibrary.com]

Figure 8 shows few periods of some typical steady-state waveforms for both converters for a constant value of the inductance L. The starting time, period and duty cycle of the kth PWM cycle are t_k, ΔT_k, and $d_k \in (0, 1)$, respectively, as shown in the bottom panel of Figure 8. We assume that the input voltage and output current are constant (at values $v_{in,\,k}$ and $i_{out,\,k}$, respectively) within the kth PWM cycle. This is reasonable, as they vary much more slowly than the PWM signal (typical values of the PWM frequency are indeed between 10^4 and 10^6 Hz). The SMPS operating condition during the kth PWM cycle is determined by $v_{in,\,k}$, $i_{out,\,k}$, ΔT_k, and d_k, which are assumed to be known or easily measurable. We also define the following time intervals:

$$\mathcal{T}_k^{ON} = \{t \in \mathbb{R} : t_k \le t < t_k + d_k \Delta T_k\}, \tag{6}$$

$$\mathcal{T}_k^{OFF} = \{t \in \mathbb{R} : t_k + d_k \Delta T_k \le t < t_{k+1}\}. \tag{7}$$

In other words, for $t \in \mathcal{T}_k^{ON}$, the PWM signal is high (ON phase) and the transistor conducts current, whereas for $t \in \mathcal{T}_k^{OFF}$, the PWM signal is low (OFF phase) and the transistor does not conduct.

During the ON phase, the inductor stores part of the electrical energy provided by the voltage source, which is then released to the load during the OFF phase. We assume that these converters always work in continuous conduction

mode (CCM), namely, the inductor current i is always strictly positive. Under this assumption, the SMPS state equations are as follows:

- buck converter

$$\begin{cases} \dfrac{di}{dt} = \dfrac{v_{in,k} - (R_L + R_{mos})i - v_{out}}{L} \\ \dfrac{dv_{out}}{dt} = \dfrac{i - i_{out,k}}{C} \end{cases} \text{for } t \in \mathcal{T}_k^{ON}, \quad \begin{cases} \dfrac{di}{dt} = \dfrac{-v_d - R_L i - v_{out}}{L} \\ \dfrac{dv_{out}}{dt} = \dfrac{i - i_{out,k}}{C} \end{cases} \text{for } t \in \mathcal{T}_k^{OFF}, \tag{8}$$

- boost converter

$$\begin{cases} \dfrac{di}{dt} = \dfrac{v_{in,k} - (R_L + R_{mos})i}{L} \\ \dfrac{dv_{out}}{dt} = \dfrac{-i_{out,k}}{C} \end{cases} \text{for } t \in \mathcal{T}_k^{ON}, \quad \begin{cases} \dfrac{di}{dt} = \dfrac{v_{in,k} - R_L i - v_d - v_{out}}{L} \\ \dfrac{dv_{out}}{dt} = \dfrac{i - i_{out,k}}{C} \end{cases} \text{for } t \in \mathcal{T}_k^{OFF}, \tag{9}$$

where L is, in general, a function of current and temperature for the reasons explained in the previous section.

If the parasitic resistances are neglected and the inductance is constant, at steady state, within the kth PWM period, the inductor current is a triangular wave with mean value $\bar{i}_k$ and ripple Δi_k, the inductor voltage v is a square wave assuming values v_k^{ON} and v_k^{OFF}, whereas the output voltage oscillates ripple around a DC value $\bar{v}_{out,k}$. The SMPS provides an ideally constant output voltage, therefore the capacitance C is chosen as a compromise between low ripple (high capacitance, according to Equations 8 and 9) and fast transient response (low capacitance).

If the inductor operates in partial saturation, the inductor current waveform assumes a cusp-like shape, as shown in Figure 9, where i is shown for different values of the converter output current i_{out}. This happens because, in the ON state, the inductor voltage is almost constant and the inductance decreases as the current increases, which implies (according to Equation 4) that also the time derivative of the inductor current increases. The same phenomenon happens in the OFF state.

At steady state, the inductor is characterized by a mean power loss p, which is responsible for a core temperature rise T_{rise} with respect to the ambient temperature T_{amb}. The temperature rise is related to the thermal dissipation characteristics of the specific component, often simply modeled through a thermal resistance[30] R_{th},

$$T_{rise} = R_{th} p. \tag{10}$$

Therefore, the core temperature T can be expressed as

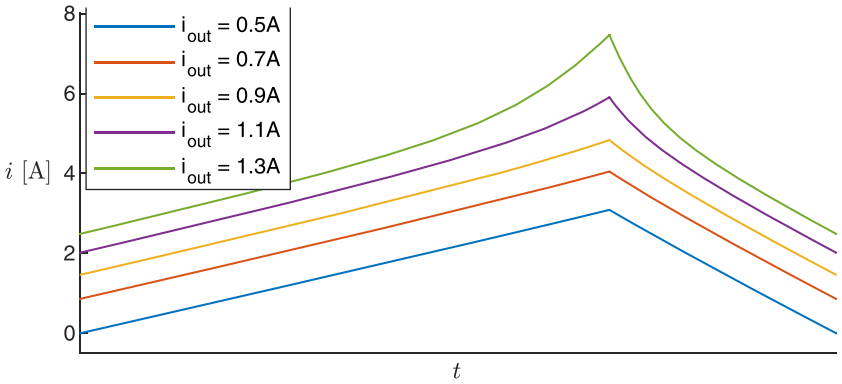

FIGURE 9 Time evolution of i during one PWM period, for different values of i_{out} [Colour figure can be viewed at wileyonlinelibrary.com]

$$T = T_{amb} + T_{rise}. \tag{11}$$

The steady-state power loss and temperature are determined by the SMPS operating condition and environmental factors, such as the ambient temperature. When one of the SMPS operating conditions (e.g., supply voltage or load current) changes, the inductor current (as well as the other electrical quantities) reaches a new oscillating steady-state value, after a fast *electrical transient*, usually lasting few PWM cycles (see Figure 10, bottom panel). If, for example, the new values of the mean current and/or ripple are higher than the previous ones, the inductor power loss is also higher and the core temperature starts rising until reaching a new steady-state value. This *thermal transient* is much slower than the electrical one and can last up to tens of minutes, depending on the thermal characteristics of the inductor. A dynamical dependence of the temperature rise on the power loss can be adopted to mimic this behavior,[31]

$$R_{th}C_{th}\frac{dT_{rise}}{dt} + T_{rise} = R_{th}p, \tag{12}$$

being C_{th} a thermal capacitance.

When the temperature increases, the differential permeability, and then the inductance, decreases (see Figure 3C). This causes a slow increase of the current ripple, as shown in Figure 10. This phenomenon is much more evident when the inductor works in partial saturation, as clearly shown also in the thermal analysis performed by Scirè et al.[32] As described in detail by Vitale et al,[31] the increase of the ripple leads in turn to a further increase of the temperature, resulting in a positive feedback, which may cause a thermal collapse of the inductor, in the absence of protection systems.

In conclusion, in response to a change in the SMPS operating conditions, the electric variables undergo both a fast electric and a slow thermal transient. Therefore, the SMPS can be considered as a *slow-fast* system.

4 | INDUCTANCE MODELS

In this section, several inductor nonlinear behavioral models are surveyed, which express the inductance as a function of the inductor current and other thermal or electrical quantities. For all models, the inductance is expressed as

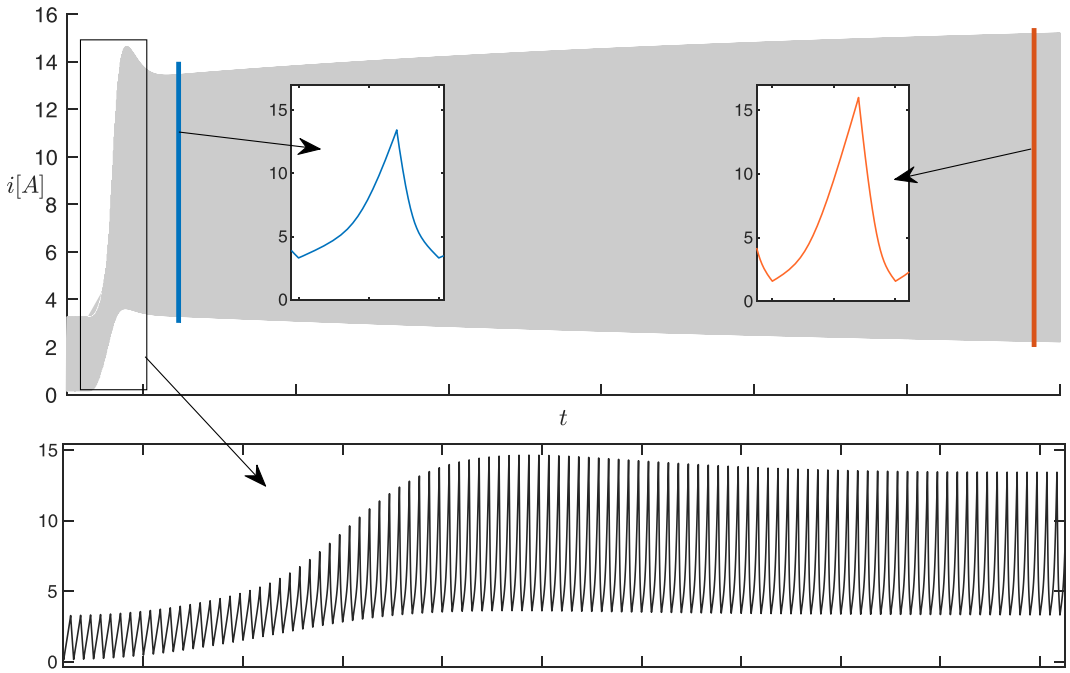

FIGURE 10 Inductor current in response to a step change of the output current. The slow thermal transient is visible in the top panel, whereas the fast electric transient is enlarged in the bottom panel [Colour figure can be viewed at wileyonlinelibrary.com]

$$L(i;\xi,x), \tag{13}$$

where i is the inductor current, ξ is a parameter that is assumed to remain constant during the PWM cycle (i.e., the core temperature), and x is the vector of the model coefficients to be identified.

Table 1 summarizes the main characteristics of the models described in the following, by indicating the kind of mathematical function, the number of coefficients, the specific parameter ξ, the adopted fitting strategy (see Section 4.1), the nature of the resulting optimization problem (quadratic programming [QP] or nonlinear programming [NLP]), and the specific circuit used for measurements. Figure 11 shows the "shape" of the L versus i curve for some relevant models.

In order not to unnecessarily complicate the notation, the same symbols may have a different meaning in different models.

Polynomial models

Simple polynomial models[33,34] express the inductance as

$$L(i;x) = \sum_{n=0}^{N} c_n i^n, \text{ with } x = [c_0, ..., c_N]. \tag{14}$$

Scirè et al[35] add a dependence on the core temperature T by expressing the inductance as

$$L(i;T,x) = \sum_{n=0}^{3} (1 + a_n T) i^n, \text{ with } x = [a_0, ..., a_3] \text{ and } \xi = T. \tag{15}$$

TABLE 1 Comparison between nonlinear behavioral inductance models, with the indication of the kind of mathematical function, the number of coefficients, the specific parameter ξ, the adopted fitting strategy, the nature of the resulting optimization problem, and the circuit where measurements are taken

Model	Function	No. coeff.	ξ	Fitting	Opt. problem	Circuit
Özkan and Hava[33]	Polyn.	4	–	L-based, Equation (30)	QP	VSC
Lullo et al.[34]	Polyn.	6	–	L-based, Equation (29)	QP	Buck
Scirè et al.[35]	Polyn.	4	T	L-based, Equation (29)	QP	Boost
Mastromauro et al.[36]	Polyn.	4	–	–	–	Inverter
Di Capua et al.[37]	Polyn.	2–3	–	Φ-based	QP	Buck
Burrascano et al.[38]	MLP	10	–	L-based (datasheet)	NLP	–
Di Capua and Femia[15]	Atan	6	T	L-based (datasheet)	NLP	Buck
Oliveri et al.[39]	Atan	7	i_{out}	Φ-based	NLP	Buck
Oliveri et al.[40]	Atan	5	p	Φ-based	NLP	Buck
Stoyka et al.[41]	Double atan	16	T	L-based	NLP	Buck
Burrascano et al.[42,43]	Hammerstein	n.a.	–	–	–	–
Oliveri et al.[44]	PWA	$2n + 1$	p	Φ-based	NLP	Buck
Mastromauro et al.[36]	PWA	3	–	–	–	Inverter
Mariethoz et al.[45]	PWA	2	–	–	–	Buck
Bizzarri et al.[46]	Atan (dynamical)	7	i_{out}	i-based	NLP	Boost
Lodi et al.[47]	Atan (dynamical)	6	p	i-based	NLP	Boost
Lodi et al.[48]	PWA (dynamical)	6	p	Φ-based	NLP	Boost
Stoyka et al.[49]	Atan (family)	5	T	L-based (datasheet)	NLP	–
Lodi et al.[50]	Atan (family)	5	p	Φ-based	NLP	Boost

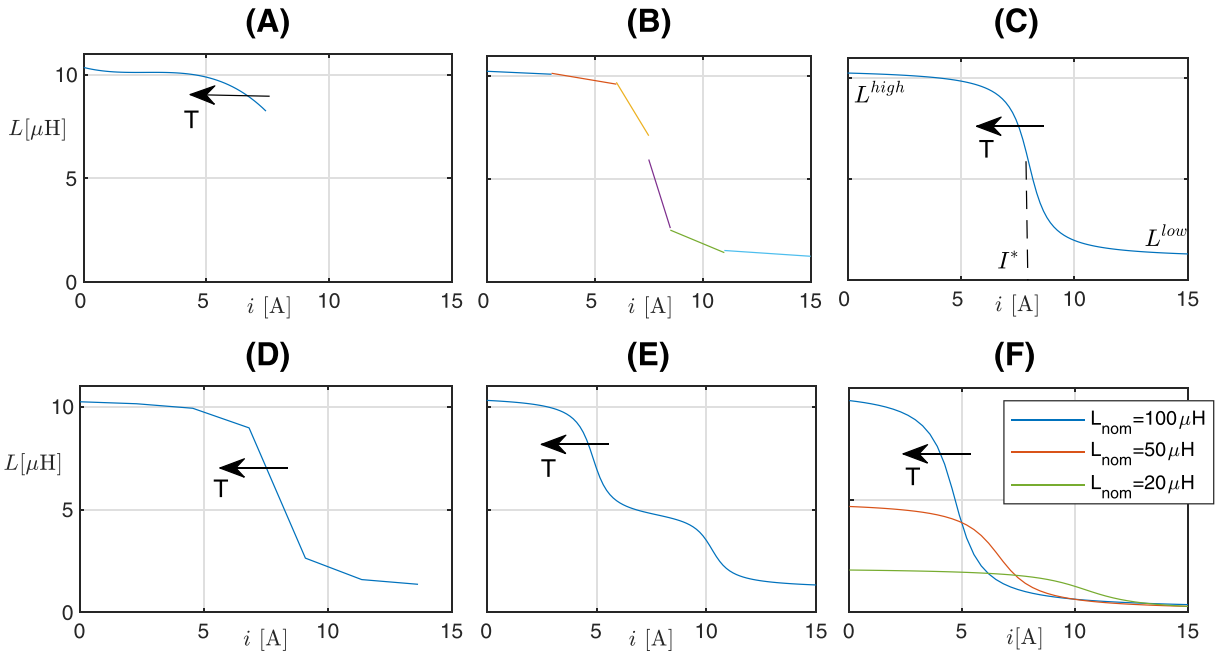

FIGURE 11 Inductance vs. current curves of different models: (A) polynomial model,[35] (B) local linear models,[37] (C) arctangent models,[15,39,40,46,47] (D) PWA model,[44] (E) double arctangent model,[41] (F) family models.[49,50] The arrows indicate how each curve moves as the core temperature increases. Each color corresponds to a different linear model, fitted to a specific operating condition (panel (B)) or to a different inductor in the family (panel (F)) [Colour figure can be viewed at wileyonlinelibrary.com]

A plot of the resulting L versus i curve is shown in Figure 11A.

Local linear and quadratic inductance models[37] are valid only for a small current swing about a bias value. The inductance is represented locally as in Equation (14) with $N=1$ (linear models) or $N=2$ (quadratic models). Several models, each with a different coefficient vector x, are identified for different SMPS operating conditions leading to a small current ripple around different bias values. Figure 11B shows examples of linear local models.

A temperature-independent polynomial model based on Volterra expansion is also proposed by Mastromauro et al.[36]

Neural models

Polynomial models are fast to evaluate, also through embedded circuits, but they are valid only for a limited current range (see Figure 11A,B). On the contrary, neural models can ideally shape any function and can therefore reproduce the whole L versus i curve, at the cost of higher computation complexity. Burrascano et al[38] exploit a multilayer perceptron (MLP) network to approximate the inductance. The MLP is composed of one input node, a single hidden layer with M neurons with threshold Θ_j and weight w_j and a single output neuron which linearly sums its inputs through weights $\alpha_j, j=1,...,M$. The inductance is therefore expressed as

$$L(i;x)=\sum_{j=1}^{M}\alpha_j\psi\left(w_j i-\Theta_j\right),\ \text{with}\ x=[\alpha_1...\alpha_M,w_1...w_M,\Theta_1...\Theta_M], \tag{16}$$

where $\psi(z)=(1+e^{-z})^{-1}$ is the sigmoid function.

Arctangent models

A model able to reproduce the whole L-vs.-i curve of ferrite-core inductors[15,39,40] is based on the following function:

$$L(i;\xi,x) = L^{low} + \frac{L^{high} - L^{low}}{2}\left\{1 - \frac{2}{\pi}\text{atan}\{\sigma(\xi)[i - I^*(\xi)]\}\right\}. \tag{17}$$

This function, plotted in Figure 11C, reflects the behavior of the differential permeability shown in Figure 3C. Parameters L^{high} and L^{low} are the horizontal asymptotes of the curve, I^* is the abscissa of its inflection point, and σ controls the slope of the curve at $i = I^*$. In particular, Di Capua et al[15] consider $\xi = T$ (core temperature) and express $\sigma(T) = (\alpha T + \beta)^{-1}$ and $I^* = \gamma T + \delta$. The coefficient vector is therefore $x = [L^{high}, L^{low}, \alpha, \beta, \gamma, \delta]$.

The core temperature is often difficult both to measure and to predict if the geometric and magnetic properties of the inductor are not known, as it often happens for commercial inductors. For this reason, some variants of the arctangent model rely on quantities that are easier to measure. Oliveri et al[39] consider $\xi = i_{out}$, σ constant and

$$I^* = \begin{cases} \alpha i_{out}^2 + \beta i_{out} + \gamma, \text{ if } i_{out} > I_{th}, \\ \alpha I_{th}^2 + \beta I_{th} + \gamma, \text{ if } i_{out} \le I_{th}. \end{cases} \tag{18}$$

The parameter vector is therefore $x = [L^{high}, L^{low}, \sigma, \alpha, \beta, \gamma, I_{th}]$. The SMPS output current i_{out} is easy to measure and is a known input in the SMPS simulator. Yet, this model is valid only for fixed values of the other SMPS operating conditions.

This model can be generalized[40] by considering $\xi = p$ and $I^* = \alpha p + \beta$, being $x = [L^{high}, L_{low}, \sigma, \alpha, \beta]$. The mean inductor power loss p is also easy to measure, as it depends on the inductor current and voltage. Different operating conditions lead to different power losses; therefore, this model can be applied for a wider range of SMPS operating conditions. However, parameters α and β depend on the thermal characteristics of the system, and therefore, they may vary if the ambient temperature or the SMPS containing the inductor change.

The arctangent model (17) is used as starting point to model ferrite-core inductors with a stepped air gap[41] (shown in Figure 12), which allows achieving a controlled decrease in inductance at large current values.[51,52]

In this case, the inductance is modeled as a double arctangent, shown in Figure 11E:

$$L(i;T,x) = L^{low,1} + \frac{L^{high,1} - L^{low,1}}{2}\left\{1 - \frac{2}{\pi}\text{atan}\{\sigma_1[i - I_1^*(T)]\}\right\} + \tag{19}$$

$$+ L^{low,2} + \frac{L^{high,2} - L^{low,2}}{2}\left\{1 - \frac{2}{\pi}\text{atan}\{\sigma_2[i - I_2^*(T)]\}\right\}, \tag{20}$$

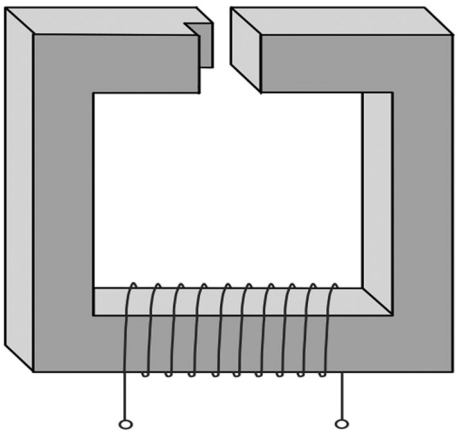

FIGURE 12 Ferrite core with stepped air gap

where all parameters are affine functions of the core temperature: $L^{low,j} = a_{1j}T + b_{1j}, L^{high,j} = a_{2j}T + b_{2j}$, $\sigma_j = a_{3j}T + b_{3j}, I_j^* = a_{4j}T + b_{4j}$, for $j = 1,2$. Coefficient vector is therefore $x = [a_{11}, a_{12}, a_{21}, a_{22}, a_{31}, a_{32}, a_{41}, a_{42}, b_{11}, b_{12}, b_{21}, b_{22}, b_{31}, b_{32}, b_{41}, b_{42}]$.

Hammerstein models

The evaluation of an arctangent function can be complex and time-consuming for low-cost embedded digital circuits. Therefore, Burrascano et al[42,43] propose approximating the arctangent function through a Hammerstein model, whose general structure relating the output y to an input x is shown in Figure 13. Terms $H_j(f)$ represent transfer functions of linear dynamical systems. The model parameters are obtained through a pulse compression identification technique, that requires applying an input chirp signal to the system. Either a current[42] or a voltage[43] is applied to an arctangent inductor model, to obtain the approximating Hammerstein model. Such signals, however, are difficult to apply to a real inductor installed on a converter.

PWA models

The main drawback of the arctangent model is its computational complexity, especially for embedded circuits. Oliveri et al[44] propose a piecewise-affine (PWA) formulation of the inductance,

$$L(i;p,x) = f^{PWA}(i - I^*(p)) \triangleq f^{PWA}(i'), \tag{21}$$

where $I^*(p) = \alpha p$ and $f^{PWA}(i')$ is a continuous PWA function, shown in Figure 11D. Function f^{PWA} is uniquely defined by N ordered knee points $i'_n, n = 1,...,N$ and by the values f_n^{PWA} at these points. The coefficient vector is $x = [i'_1,...,i'_N, f_1^{PWA}..f_N^{PWA}, \alpha]$. The evaluation of the PWA model is more than one order of magnitude faster compared to the evaluation of the arctangent model, on a low-cost microcontroller.

Moreover, if v and p are constant, the differential equation (4) $\frac{di}{dt} = \frac{v}{L(i;p,x)}$ has an analytical solution and the inductor current can be computed analytically, based on the inductor voltage.

Simple PWA inductance models are also proposed by Mastromauro et al[36] and Mariethoz et al.[45]

Dynamical models

The arctangent and PWA models depending on i_{out} or p implicitly consider the effect of the temperature on the permeability, as different values of i_{out} or p lead to different core temperatures at steady state. However, since this

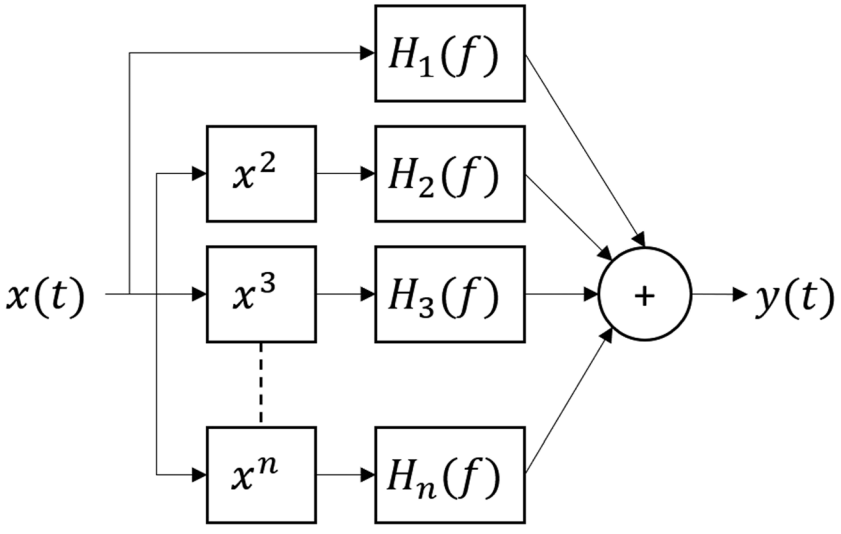

FIGURE 13 General structure of the Hammerstein model

relationship is only valid at thermal steady state, these models cannot be applied during thermal transients. This drawback is overcome by dynamical models,[46-48] where parameter I^* becomes the state variable of a dynamical system. A linear first-order system, whose time constant τ is chosen in order to mimic the slow temperature evolution, proved to be sufficiently accurate,

$$\tau \frac{dI^*}{dt} = I^*_\infty - I^*(t). \tag{22}$$

In this case, I^* and therefore L depend explicitly on time. The steady-state value I^*_∞ is defined as[46]

$$I^*_\infty(i_{out}) = \alpha i^2_{out} + \beta |i_{out}| + \gamma, \tag{23}$$

or[47,48]

$$I^*_\infty(p) = \alpha p + \beta, \tag{24}$$

being α, β, and γ model parameters. The resulting value of I^* is used in Equation (17)[46,47] or in Equation (21).[48]

Family models

Inductors of the same family share the same magnetic core and differ for the number of turns n in the windings, which determines their nominal inductance L_{nom}.

A normalized version of the arctangent model can be used for all inductors in a given family.[49,50] The inductance of the jth inductor of the family is expressed as[49]

$$L_j(i,T,x) = L_{nom,j}c_1 + \frac{L_{nom,j} - L_{nom,j}c_1}{2}\left\{1 - \frac{2}{\pi}\text{atan}\left[c_2 X_j(T)\left(i - \frac{1}{X_j(T)}\right)\right]\right\} \tag{25}$$

or[50]

$$L_j(i,p,x) = L_{nom,j}c_1 + \frac{L_{nom,j} - L_{nom,j}c_1}{2}\left\{1 - \frac{2}{\pi}\text{atan}\left[c_2\sqrt{L_{nom,j}}\left(i - \frac{c_3(p)}{\sqrt{L_{nom,j}}}\right)\right]\right\}. \tag{26}$$

Stoyka et al[49] consider $\xi = T$ and $X_j(T) = \gamma_j T + \delta_j$. Coefficients c_1 and c_2 are common to all inductors within the family, whereas coefficients $L_{nom,j}, \gamma_j$, and δ_j are specific for each single inductor. Lodi et al[50] consider instead $\xi = p$, and $c_3(p) = \alpha p + \beta$. Coefficients c_1, c_2, α, and β are common to all inductors within the family. The only specific coefficient is the nominal inductance $L_{nom,j}$ of the specific inductor, which is always available in the manufacturer datasheet. Some L versus i curves for different inductors of the same family are shown in Figure 11F. As already explained in Section 2.1, the higher the inductance (i.e., the number of turns), the lower the current value from which the inductance starts decreasing.

4.1 | Model fitting

The identification of the parameters of a given model is performed through the solution of an optimization problem, whose cost function $J(x)$ is based either on measurements or datasheet information,

$$x = \underset{x}{\operatorname{argmin}} J(x). \tag{27}$$

Measurements are usually performed directly on the SMPS the inductor is mounted on so that the models are identified based on the real inductor current and voltage waveforms. We denote as $\hat{\imath}_{kj}$ and $\hat{v}_{kj}$ the samples of the inductor current and voltage, respectively, measured at times t_{kj} in the kth PWM cycle (see Figure 14), with $j \in \mathcal{J}$ and $k \in \mathcal{K}$, being $\mathcal{J}$ and $\mathcal{K}$ two sets of indices. We also assume that the value of the parameter $\xi = \xi_k$ in the kth PWM cycle is known.

To properly identify the models, measurements should be taken for different SMPS operating conditions. A useful, yet expensive, tool that allows accomplishing this task automatically is the MADMIX[53] device, embedding a buck converter whose inductor can be easily changed, to characterize different components.

The majority of models described above are identified through one of the following fitting strategies, based on least-squares optimization, even if any identification technique could be applied, in principle, to any model.

4.1.1 | Inductance-based fitting

In the inductance-based fitting strategy, the cost function is defined as

$$J(x) = \sum_{k \in \mathcal{K}} \sum_{j \in \mathcal{J}} \left[\hat{L}_{kj} - L(v_{kj}, \xi_k, x)\right]^2, \tag{28}$$

where $L(\hat{\imath}_{kj}, \xi_k, x)$ is the value of inductance returned by the model for $i = \hat{\imath}_{kj}$, $\xi = \xi_k$ and coefficient vector x, whereas $\hat{L}_{kj}$ can be either retrieved from the datasheet, on the L versus i curve obtained with $\xi = \xi_k$ for current $i = \hat{\imath}_{kj}$, or computed based on current and voltage measurements. In the latter case, the possible alternatives are

$$\hat{L}_{kj} = \left.\frac{\hat{v}}{d\hat{\imath}/dt}\right|_{i=\hat{\imath}_{kj}, \xi=\xi_k} \tag{29}$$

or

$$\hat{L}_{kj} = \left.\frac{d\hat{\Phi}}{di}\right|_{i=\hat{\imath}_{kj}, \xi=\xi_k}. \tag{30}$$

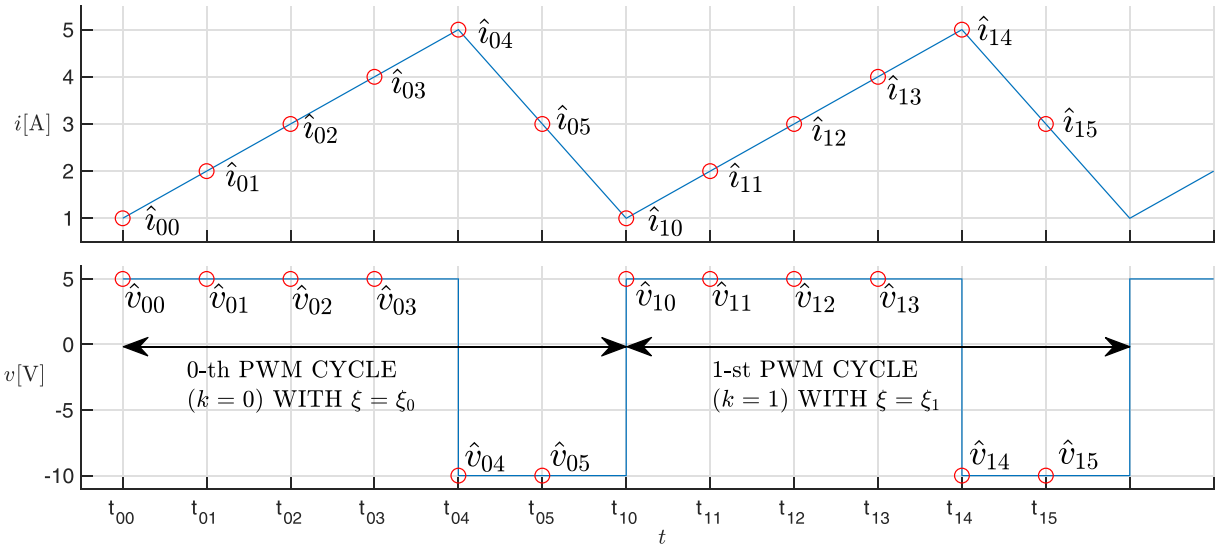

FIGURE 14 Example of measurements of inductor current and voltage on 2 PWM cycles ($k = 0$ and $k = 1$). For each cycle, six measurements are taken ($j = 0, \ldots, 5$). In this case, $\mathcal{K} = \{0, 1\}$ and $\mathcal{J} = \{0, 1, 2, 3, 4, 5\}$ [Colour figure can be viewed at wileyonlinelibrary.com]

In both cases, the derivative must be computed numerically, based on samples $\hat{\imath}_{kj}$ and $\hat{\Phi}_{kj}$ of the current and flux. Flux $\hat{\Phi}_{kj}$, corresponding to $i = \hat{\imath}_{kj}$ and $\xi = \xi_k$, is evaluated by numerically computing the following integral:

$$\hat{\Phi}_{kj} = \int_{t_{k0}}^{t_{kj}} \hat{v}(t)dt. \tag{31}$$

Obtaining $\hat{L}_{kj}$ from the datasheet is not always possible, as the L versus i curves may be unavailable or limited to the linear and partial saturation regions only. Moreover, these curves are often obtained by imposing small-amplitude sinusoidal voltage and current with a bias; therefore, the actual inductance obtained when the inductor operates on the SMPS may be different. On the other hand, computing the time derivative of the measured inductor current, as in Equation (29), may lead to large inaccuracies, due to measurement noise. This issue can be overcome by resorting to a flux-based fitting.

4.1.2 | Flux-based fitting

In the flux-based fitting strategy, the cost function is defined as

$$J(x) = \sum_{k \in \mathcal{K}} \sum_{j \in \mathcal{J}} \left[\hat{\Phi}_{kj} - \Phi(\hat{\imath}_{kj}, \xi_k, x)\right]^2. \tag{32}$$

Within the kth period, the flux $\hat{\Phi}_{kj}$ is defined in Equation (31), whereas $\Phi(t_{kj}, \xi_k, x)$ is computed by integrating the inductance value returned by the model, according to Equation (4):

$$\Phi(t_{kj}, \xi_k, x) = \int_{i_{k0}}^{i_{kj}} L(i, \xi_k, x)di. \tag{33}$$

The complexity of this integral depends on the adopted model, but often it admits an analytical solution.

By contrast with the inductance-based fitting procedure, here an integral is computed instead of a derivative, which automatically filters the measurement noise and therefore turns out to be more accurate.

4.1.3 | Current-based fitting

Usually, the inductance model is exploited within an SMPS simulator to correctly reproduce the inductor current waveform, based on the applied voltage. In this case, it is more practical to look for the coefficient vector x such that the error between the measured and simulated current is minimum. In the current-based fitting strategy, the cost function is defined as

$$J(x) = \sum_{k \in \mathcal{K}} \sum_{j \in \mathcal{J}} \left[\hat{\imath}_{kj} - i(t_{kj}, \xi_k, x)\right]^2, \tag{34}$$

where $i(t_{kj}, \xi_k, x)$ is the current obtained at time t_{kj} for $\xi = \xi_k$ by exploiting the inductance model with coefficient vector x. The current can be obtained either by simulating the whole SMPS or the single inductor.

Performing a whole SMPS simulation to evaluate the cost function for a given vector x can be time-consuming, due to the slow-fast nature of the SMPS (see Figure 10). The *envelope following method*[54-56] is a suitable simulation strategy for slow-fast circuits. The inductor voltage measurements are not required, as the simulator takes in input the SMPS operating conditions, but the whole SMPS model must be accurate to obtain a reliable inductor current prediction.

Instead of simulating the whole SMPS, the inductance model can be exploited to predict the inductor current, based on the inductor voltage, through Equation (4).[57] The inductor voltage at electrical steady state can be indeed obtained based on the SMPS operating conditions. Simulating only the inductor is much faster than considering the whole SMPS and, if polynomial or PWA inductance models are exploited, the current can be obtained analytically. However, the electrical transients cannot be reproduced.

4.2 | Discussion

All surveyed models aim at reproducing, at least partially, the physical behavior of inductors working in saturation, as summarized in Section 2.1. The simpler models do not account for the effects of the temperature and only reproduce the decrease of the differential inductance as the current increases. By contrast, the more detailed models are more general as they also consider the dependence of the curve L versus i on the core temperature. The magnetic hysteresis is usually considered as a negligible effect and is not taken into account by any of the surveyed models.

The models that only depend on inductor current, that is, not relying on ξ (see Table 1), are valid only for a limited range of core temperatures, such that the permeability of the material does not change. They may be appropriate also for materials with a low dependency on temperature, for example, nanocrystalline cores. These models can be therefore exploited for the SMPS operating conditions which guarantee the same temperature. On the contrary, models taking into account the core temperature can be applied for any operating condition, both at steady-state and during thermal and electric transients. Nevertheless, these models have two main drawbacks: (i) their identification requires measuring the inductor core temperature, which is not always possible, especially for commercial inductors; (ii) when these models are used for SMPS simulation, the evolution of the core temperature must be also simulated, based on the SMPS operating conditions and ambient temperature. An accurate thermal model is often difficult to obtain. Instead of directly considering the core temperature, some models take in input the SMPS output current i_{out}, which is much easier to measure and is a known parameter in SMPS simulators. Yet, these models are valid only for fixed values of the other SMPS operating conditions. This issue is overcome by models taking in input the inductor mean power loss, which is also easier to measure compared to the core temperature, as it depends on the inductor current and voltage. Different operating conditions lead to different power losses; therefore, the models can be applied for a wider range of SMPS operating conditions. For simulation purposes, however, an accurate power loss model is required, relating p to the SMPS operating conditions (see Section 5). The effect of the temperature on the permeability is considered implicitly by these models, as different values of i_{out} or p will lead to different core temperatures at steady state (see Equation 10), but this relationship is only valid at thermal steady state. Therefore, these models cannot be applied during thermal transients. A solution is to consider a dynamical model, where the parameters do not depend on the output current or power loss instantaneously, but through a first-order linear dynamical system, with a time constant chosen to mimic the slow temperature changes.

The models not depending on the core temperature share a common drawback. The relationship between the SMPS operating conditions (or inductor power loss) and the core temperature depends on the specific SMPS, the ambient temperature, and the possible presence of heat dissipation devices. Therefore, each model is tailored to a specific SMPS for fixed environment conditions. Lodi et al[58] show how the accuracy of each parameter of the dynamical model of Equations (22) and (24) affects the overall accuracy in reproducing the inductor current. The results show that the identification of some model parameters is more critical than for others. Therefore, if the same inductor is moved to a different SMPS, the model accuracy can be compromised.

From a computational standpoint, polynomial models[33-35,37] are fast to evaluate and easy to identify as they are linear with respect to their coefficients, which implies that the cost function $J(x)$ is quadratic for inductance-based or flux-based identification. On the other hand, these (local) models are not able to reproduce the whole L versus i curve. The arctangent-, PWA-, and MLP-based models are more general, but they are more complex to evaluate and their fitting requires the solution of an NLP problem, which can have local minima.

The PWA and MLP models are more flexible as they can ideally fit any curve, including the inductance of stepped-gap cores. Yet, they require many measurements to be identified and they do not have extrapolation capabilities.

Finally, the polynomial and PWA models allow computing the inductor current analytically, based on the inductor voltage.

5 | LOSS MODELS

Assuming that the inductor current and voltage are periodic signals with period ΔT (frequency f), the inductor mean total power loss p over the period is defined as

$$p = \frac{1}{\Delta T} \int_{t}^{t+\Delta T} v(\tau) i(\tau) d\tau. \tag{35}$$

If the inductor is modeled through Equation (4), the above integral is zero, thus resulting in a conservative component. Real inductors are characterized by a nonnegligible power loss due to both the core (owing to the aforementioned hysteresis loop and eddy currents) and the windings (owing to the wire resistivity, skin effect, and proximity effect). Therefore, to properly model inductors, it is necessary to combine the inductance model with a power loss model.

The total inductor power loss can be split as $p = p_{core} + p_{wind}$.[59-61] The term p_{core} includes the loss in the magnetic core, which comprises hysteresis loss (the area of the hysteresis loop is proportional to the dissipated energy), eddy current loss, and excess eddy current loss;[62] all terms depend on the core temperature, material, shape, and on the harmonic content of the applied magnetic field. The term p_{wind} accounts for the power loss in the inductor windings, due to ohmic loss, skin effect, and proximity effect.

However, core and winding loss cannot be easily measured as separate contributions in SMPS applications[63] since the geometrical properties of the inductor, such as winding turn number, magnetic path length, core, and winding cross-sectional areas are not always disclosed for commercial inductors. Moreover, all methods for the computation of p_{core} and p_{wind} rely on magnetic quantities. Some inductor manufacturers, however, provide tools for the estimation of winding and core loss.

As an alternative, the power loss can be split into DC and AC components. By considering the inductor current and voltage as $i(t) = i_{dc} + i_{ac}(t)$ and $v(t) = v_{dc} + v_{ac}(t)$, being i_{dc} and v_{dc} constant values and $i_{ac}(t)$ and $v_{ac}(t)$ periodic signals with zero mean, the power loss can be evaluated as

$$p = \frac{1}{\Delta T} \int_{t}^{t+\Delta T} (v_{dc} + v_{ac})(i_{dc} + i_{ac}) dt = \underbrace{\frac{1}{\Delta T} \int_{t}^{t+\Delta T} v_{dc} i_{dc} dt}_{p_{dc}} + \underbrace{\frac{1}{\Delta T} \int_{t}^{t+\Delta T} v_{ac} i_{ac} dt}_{p_{ac}}, \tag{36}$$

and the separate contributions can be computed based on the DC and AC components of the inductor voltage and current. DC and AC components of the power loss can be easily measured through the inductor voltage and current; therefore, behavioral models relating the loss to easy-to-measure electrical quantities can be developed, which can be easily included in SMPS simulators to forecast the inductor power loss.

In the next two sections, the most relevant models for the computation of p as $p_{wind} + p_{core}$ or $p_{dc} + p_{ac}$ are summarized.

5.1 | Winding (copper) and core (iron) loss

The inductor *winding loss* due to the wire resistivity is expressed as[59]

$$p_{wind,dc} = R_{dc} i_{rms}^2, \tag{37}$$

where i_{rms} denotes the root mean square value of $i(t)$ over one period and R_{dc} is the temperature-dependent DC resistance, usually provided by the manufacturers. A linear dependence of the resistance on the temperature is typically assumed by the manufacturers,[64]

$$R_{dc}(T) = R_{dc}(25^\circ\mathrm{C})[1+\rho(T-25^\circ\mathrm{C})], \tag{38}$$

being ρ the thermal coefficient, equal to $3.85 \cdot 10^{-3\circ}\mathrm{C}^{-1}$ for copper. This loss term is easily reproduced by adding to the inductor a series resistance $R_L = R_{dc}$. The loss due to skin and proximity effects only depends on the RMS value of the AC component of the inductor current, through the AC resistance R_{ac}:

$$p_{wind,ac} = R_{ac} i_{ac,rms}^2, \tag{39}$$

where R_{ac} increases with the excitation frequency and is not always provided by the manufacturers. Several methods are proposed in the literature[65] for accurate evaluation of R_{ac}. Many of them require the knowledge of physical and geometrical properties of the windings, which are not always disclosed by manufacturers. The global winding loss can be evaluated as $p_{wind} = p_{wind,dc} + p_{wind,ac}$.

There is vast literature about *core loss* evaluation. The proposed methods can be split into three categories:[66-68] (i) loss separation approach, where magnetic loss is computed as the sum of eddy current loss, hysteresis loss, and excess eddy-current loss; (ii) hysteresis approach, relying on hysteresis models such as Preisach[69] or Jiles-Atherton[70] models; (iii) empirical approach, mainly based on the Steinmetz equation.[71] The empirical models are the easiest to identify and evaluate. For this reason, inductor manufacturers usually provide the parameters of the Steinmetz equation in the datasheets. They commonly express the effective core loss p_{core} as the product of the core loss per unit volume $p_{core,\,v}$ and the core volume, assuming a periodic magnetic field $B(t)$ with peak value B_{pk} and mean value B_{dc}.

In the original formulation[71] of the Steinmetz equation, referred to as standard Steinmetz equation (SSE), the core loss per volume is expressed as

$$p_{core,v} = k f^{\alpha} B_{pk}^{\beta}. \tag{40}$$

Coefficients k, α, and β depend on core material and temperature and are usually provided in the datasheets of magnetic cores.[29,59,72,73] The peak field B_{pk} can also be expressed as a function of the inductor current ripple,[15,72] which is easier to measure,

$$B_{pk} = c_1 \Delta i. \tag{41}$$

The SSE is valid only for unbiased ($B_{dc} = 0$) sinusoidal fields (and then voltages). The accuracy is still acceptable for square voltage waves with duty cycle 0.5, but it becomes very poor for duty cycles 0.05 or 0.95.[74]

Several variants (the most relevant of which are summarized in Appendix A.1) of the Steinmetz equation have been proposed in the literature, that allow accounting for nonsinusoidal inputs, possibly with bias, so that they can be applied also in the saturation region.

5.2 | DC and AC loss

If measurements of the inductor current and voltage are available, then p_{dc} and p_{ac} can be computed through Equation (36). However, if the SMPS is simulated, inductor voltage and current are related to each other through the inductance and also through the (unknown) power loss. Therefore, models which allow expressing the power loss based on easy-to-measure quantities are necessary.

The DC component of the power loss is only due to the mean value of the inductor current and can be expressed through the inductor DC resistance R_{dc} as

$$p_{dc} = R_{dc} i_{dc}^2. \tag{42}$$

Some behavioral models have been proposed which express the AC loss as a function of measurable electrical quantities. Stoyka et al[63] exploit a genetic programming algorithm combined with multiobjective optimization to formulate the following behavioral model for p_{ac},

$$p_{ac} = b_0 e^{-b_1 f} v_{eq}^{b_2} + b_3 v_{eq}^2, \tag{43}$$

where

$$b_k(i_{dc}) = a_{k0} e^{a_{k1} i_{dc}} + a_{k2} i_{dc} + a_{k3},\ k = 0, ..., 3. \tag{44}$$

Parameters a_{jk} $(j, k = 0, ..., 3)$ are obtained through the solution of an NLP problem, based on measurements of p in the SMPS. The dependence of parameters b_k on the mean current i_{dc} allows taking into account the effect of saturation.

Simplified representations are adopted in other works, valid only for a limited set of operating conditions. Lodi et al[48] express p_{ac} only in terms of the RMS value of the inductor current as

$$p_{ac} = \alpha i_{rms}^2, \tag{45}$$

where α is a fitting parameter. In a slightly more general formulation,[47] p_{ac} also depends on the duty cycle d,

$$p_{ac} = (\alpha d + \beta) i_{rms}^2. \tag{46}$$

All these models rely on both some SMPS operating conditions (f, d) and electrical quantities (i_{dc}, v_{eq}, i_{rms}), which can be easily monitored during SMPS simulation.

6 | APPLICATIONS

The inductance, power loss, and thermal models described in the previous sections can be exploited for several purposes, in particular:

- predicting the inductor current profile (or only the current ripple), based on the SMPS operating conditions;
- selecting the best saturating inductor which satisfies the SMPS design specifications;
- online monitoring the inductor current ripple, power loss, temperature rise, or other relevant quantities, not directly measurable;
- controlling the SMPS through model-based techniques.

6.1 | Inductor current prediction

The time evolution of the inductor current can be obtained by simulating either the whole SMPS, where the linear inductor is replaced by one of the nonlinear inductance/loss models, or only the single inductor. The current prediction is useful for design purposes, to assess that the SMPS fulfills the specifications.

6.1.1 | Whole SMPS simulation

Different levels of accuracy can be selected for the simulation of the whole SMPS. In the simplest configuration (Figure 15A), the inductance only depends on i, and only the DC winding loss is reproduced, using a constant series resistor with resistance $R_L = R_{dc}$. This kind of simulation is accurate only for a limited set of operating conditions, leading to negligible variations of the core temperature. A much more detailed circuit (see Figure 15B) considers a temperature-dependent inductance model or a loss-dependent dynamical inductance model and a series resistance R_L which varies according to the actual inductor power loss. In this case, power-loss and/or thermal models are combined with the inductance model, leading to a simulation accurate for a wider range of operating conditions. In the surveyed works, different simulators are exploited: Simulink,[37] PSIM,[19,40,41] and PAN.[46,75-77] The simulation of the whole SMPS allows reproducing both the fast electrical transients and the slow thermal transients, provided that a temperature-dependent or a dynamical inductance model is exploited. In this case, a slow-fast system must be simulated which may

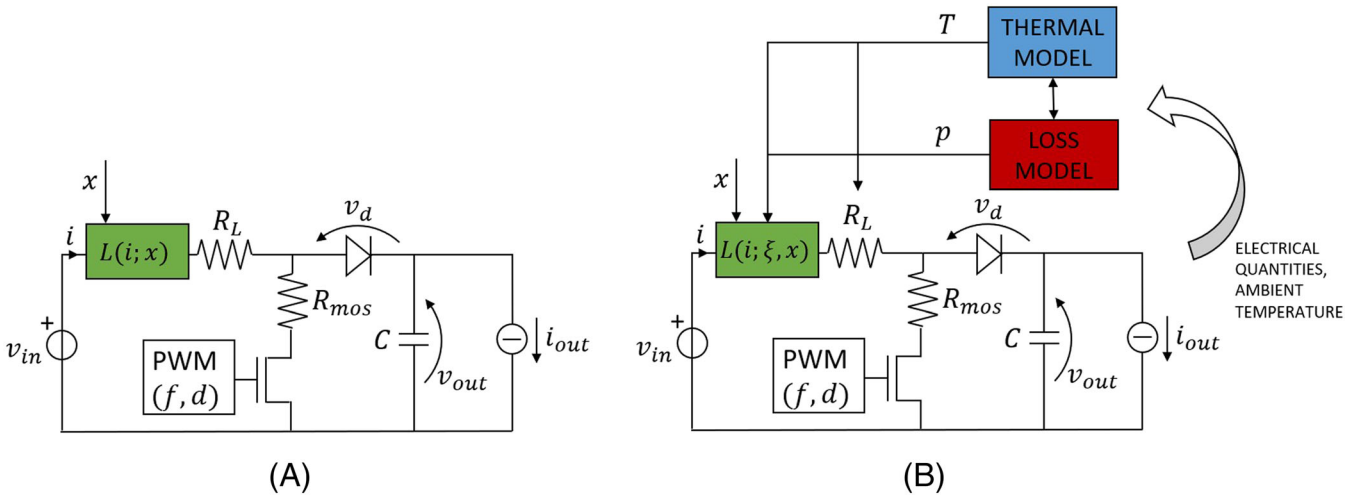

FIGURE 15 Simulation circuit in the simplest (A) and more detailed (B) configuration [Colour figure can be viewed at wileyonlinelibrary.com]

be time-consuming, as a small simulation step (in the order of nanoseconds) must be used to capture the inductor current dynamics, but the thermal transients can last up to minutes. The *envelope-following method*[54-56] permits a sensible reduction of the simulation times.

6.1.2 | Single inductor simulation

If one is interested in reproducing the inductor current at steady-state, without capturing the electrical transients, the single inductor can be simulated instead of the whole SMPS. During the ON (OFF) phase, the inductor voltage can be reasonably approximated through its mean value $\overline{v}^{ON}$ ($\overline{v}^{OFF}$), which can be calculated based on the SMPS Kirchhoff's laws. Also, the mean inductor current $\bar{\imath}$ over the PWM period can be obtained through the circuit equations. Let us consider the ON phase (similar considerations apply for the OFF phase), with $t \in [t_k, t_k + d_k \Delta T_k)$, where $v(t)\overline{v}_k^{ON}$. The inductor descriptive equation is

$$\overline{v}_k^{ON}(t) = L(i(t);\xi,x)\frac{di}{dt}. \tag{47}$$

This nonlinear differential equation can be solved by separating variables as

$$\int_{t_k}^{t} \overline{v}_k^{ON}(\tau)d\tau = \int_{i(t_k)}^{i(t)} L(i;\xi,x)di. \tag{48}$$

Therefore,

$$\overline{v}_k^{ON}(t - t_k) = \int_{i(t_k)}^{i(t)} L(i;\xi,x)di. \tag{49}$$

By solving the right-hand side integral, this equation provides $i(t)$ as a function of $\overline{v}_k^{ON}$ (which is known) and of the initial current $i(t_k)$ (which is unknown, in general). Di Capua et al[15] solve analytically the integral by exploiting the temperature-dependent arctangent model of Equation (17). However, $i(t)$ cannot be obtained explicitly, being the resulting equation transcendental, but it can be computed numerically through, for example, a Newton–Raphson

algorithm. A good representation of the inductor current can be obtained by calculating i in only five points, marked with red dots in Figure 16. A guess value is assigned to the (unknown) initial current $i(t_k)$ (point 1), and current i $(t_k + d_k\Delta T_k)$ (point 5) is evaluated by solving Equation (49). The tangents to the curve at these two points (green dashed lines) are computed through Equation (47) and their intersection provides the time instant t' where point 3 is evaluated. The procedure is repeated to obtain point 2 (based on the tangents on points 1 and 3) and point 4 (based on the tangents on points 3 and 5). The same procedure is then applied for the OFF phase. Based on the resulting estimated current values, the mean current can be computed and compared with the (known) real value. The whole algorithm is iterated by modifying the initial guess $i(t_k)$ until the error between the estimated and the real mean current falls below a given threshold.

This strategy is exploited in several other works[15,16,57,78] and is also generalized for the case of discontinuous conduction mode (DCM) operation.[79]

A similar iterative method is adopted in other papers,[80-82] where the current waveform is computed through successive approximations.

Oliveri et al[44] solve Equation (49) by exploiting the PWA inductance model of Equation (21). So doing, $i(t)$ can be computed explicitly based on $i(t_k)$ and $\overline{v}_k^{ON}$.

Instead of exploiting an inductance model, Stoyka et al[61] propose a model which directly relates the current ripple Δi_k in the kth PWM cycle to the switching frequency f_k, the mean inductor current $\bar{\imath}_k$, and the equivalent charging voltage

$$v_{eq,k} = d_k \overline{v}_k^{ON}. \tag{50}$$

By resorting to multiobjective genetic programming, the following formula is proposed:

$$\Delta i_k = b_0 f_k^{b_1} v_{eq,k}^{b_2}, \text{ with } b_j = a_{j0} e^{a_{j1}\bar{\imath}} + a_{j2}, j = 0,1,2, \tag{51}$$

where parameters a_{jh} $(j,h = 0,1,2)$ are determined by solving an NLP problem based on measurements of the inductor current ripple and operating conditions. By exploiting this model, it is not possible to obtain the whole current profile, but only the ripple value.

6.2 | SMPS design

In the SMPS design process, the choice of the inductor is crucial, as it determines the current ripple, temperature rise, and power loss, which affect the overall converter efficiency. Moreover, the inductor is usually the bulkiest component, strongly influencing the SMPS power density. Traditionally, the inductor is chosen such that constraints on the current

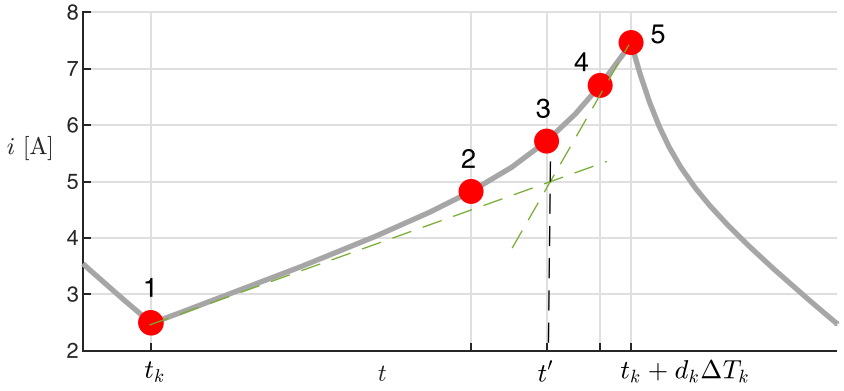

FIGURE 16 Points (red dots) used to reconstruct the steady-state inductor current waveform (gray curve) with the method proposed by Di Capua et al.[15] The dashed lines are the tangents used to obtain point 3 based on points 1 and 5 [Colour figure can be viewed at wileyonlinelibrary.com]

ripple, temperature rise, and power loss are met, ensuring that the component always works in its linear region, where the inductance can be considered constant and weakly dependent on the core temperature. In this case, the aforementioned quantities can be estimated based on datasheet information or through simple equations. To exploit smaller and lighter inductors, they should be allowed to work in partial saturation, which makes the design procedure much more complex, owing to the nonlinear behavior and strong temperature dependence of the component.

The techniques described in the following help in selecting, on the one hand, the optimal inductor such that SMPS design specifications are met for given operating conditions, on the other hand, the operating conditions such that a given inductor fulfills the design specifications.

6.2.1 | Selection of the optimal inductor

Di Capua et al[16,78] propose an iterative algorithm that, given the SMPS operating conditions, provides an estimate of the inductor current ripple Δi, mean power loss p, and temperature rise T_{rise} with respect to the ambient temperature. Once a component is fully characterized, that is, the inductance and loss model parameters and the thermal resistance are known, it is possible to assess if, for the relevant SMPS operating conditions, the inductor meets the SMPS design specifications, for example, the following constraints are fulfilled:

$$p \le p_{max},\ \Delta i \le \Delta i_{max},\ T_{rise} \le T_{rise,max}. \tag{52}$$

In the work by Di Capua et al., the current waveform and ripple are obtained through the algorithm[15] described in Section 6.1, the winding loss through Equation (37), the core loss through the Steinmetz equation by exploiting Equation (41), and the temperature rise through Equation (10). However, different inductance/loss/temperature models could be exploited and additional design constraints could be verified. With this approach, during SMPS design, it is possible to select the inductors (also working in partial saturation) that allow meeting the SMPS specifications and to choose the smallest/lightest one among these. The main drawback is that all inductors in the considered set must be fully characterized a priori.

Other papers[49,50,61] focus instead on inductors within a family (i.e., with the same core), by exploiting the family models described in Section 4. In this way, only a few inductors within each family should be characterized, to derive a model valid for all components of the same family.

Lodi et al[50] exploit the family model in Equation (26) and a DC/AC loss model within an SMPS simulator, to evaluate the inductor current ripple and power loss as a function of the nominal inductance (which characterizes each inductor within a family), for different values of the SMPS output current.

The current ripple versus nominal inductance is shown in Figure 17A; the arrow indicates the increasing direction of the output current. For low values of i_{out} (bottom curves) the inductor works in the linear region, and the ripple decreases monotonically as L_{nom} increases, independently on i_{out}. For higher values of i_{out}, the ripple reaches a minimum and then starts increasing again, as L_{nom} increases. When the inductor works in saturation, then, the current ripple does not depend monotonically on the nominal inductance and is also influenced by the output current, as it determines the working point on the L versus i characteristics. The curve in Figure 17B represents the obtained values of p and Δi for a given output current, leading to inductor saturation. As the nominal inductance increases, the curve is traveled as indicated by the black arrow. Only inductance values corresponding to the thick portion of the curve (Pareto frontier) are good design choices, balancing current ripple and power loss. The selection of an inductor with higher nominal inductance (e.g., red dot) would give the same ripple but a higher power loss compared to an inductor with lower nominal inductance (e.g., green dot). This technique should be extended to a wider range of operating conditions to be effectively applied for SMPS design.

6.2.2 | Selection of the operating conditions

Another paper[49] introduces the concept of *real operating area* (ROA). The ROA includes all possible values of the mean inductor current $\bar{\imath}$ and volt-second integral $\lambda = \Delta T v_{eq}$ which can be applied to the inductor, such that its resulting current ripple is lower than a given threshold. The normalized operating area (NOA), valid for all inductors within a family, is first obtained through SMPS simulations, by exploiting the normalized family model of Equation (25). Given

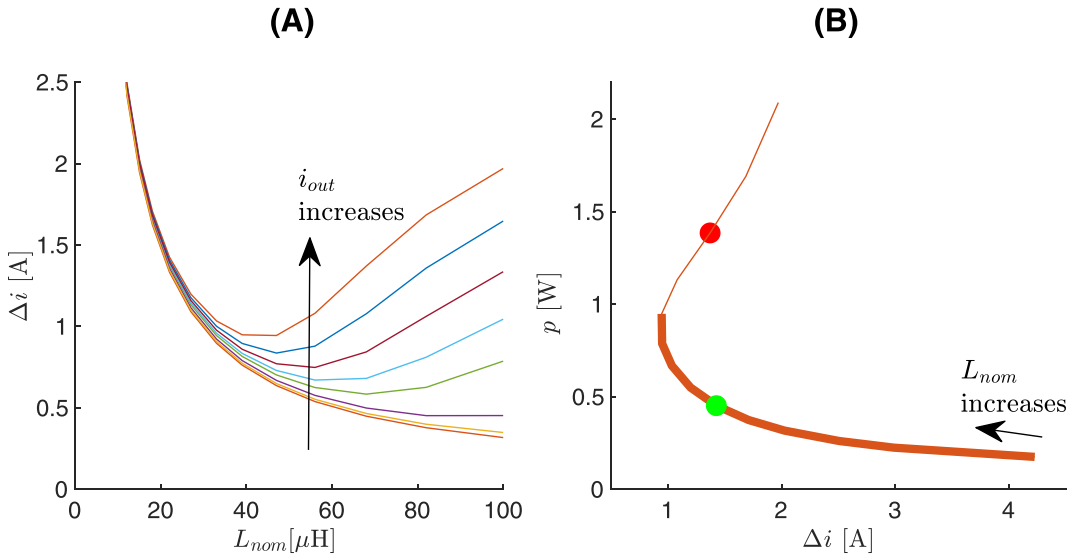

FIGURE 17 Relationship between current ripple and nominal inductance for different values of the SMPS output current (A). Relationship between ripple and power loss (B) corresponding different nominal inductance values, for a given output current. The thick portion of the curve is the Pareto frontier [Colour figure can be viewed at wileyonlinelibrary.com]

the NOA for a given family, it is possible to get the ROA of the single inductors, through proper scaling, without performing any additional simulations. In Figure 18A, the boundaries of different ROAs for a single inductor are shown. Each color corresponds to a different value of the current ripple threshold, whereas each line style to a different core temperature. If the SMPS is designed such that the mean inductor current and the volt-second integral are below a given curve, then the corresponding specification on the current ripple will be satisfied.

The same authors generalize these concepts through the constrained operating area[61] (COA) on a three-dimensional space, which includes the values of the applied switching frequency f, equivalent voltage v_{eq}, and mean current $\bar{\imath}$ such that the current ripple, total power loss, and surface temperature lie under given limits. The intersection of the volumes bounded by the three surfaces in Figure 18B is the COA for a specific inductor. These surfaces represent constraints on current ripple, power loss, and core temperature.

6.3 | SMPS online monitoring

The models described in the previous sections can be exploited for online estimating some quantities, whose direct measurement is expensive, noisy, or even not possible. In particular, monitoring current ripple, temperature rise, and power loss is important to assess if the converter is operating safely and efficiently.

To this aim, observers can be designed which exploit both measurements and models. Voltages are usually easy to measure, whereas the measurement of current is often an issue.[83,84] Shunt resistors can be exploited, which are very simple but have low accuracy, modify the circuit and increase the power loss. Mirroring circuits are sensitive to electromagnetic interference and also exhibit low accuracy. Hall effect sensors do not have these disadvantages, but they are expensive. In any case, all these current sensing techniques add noise to the system and increase the overall converter power consumption, size, and cost.[85]

A couple of observers are available[48,86] suitable for SMPSs with saturating inductors. The inputs and outputs of these observers and their connection to the boost converter are shown in Figure 19.

The first estimator[48] samples the SMPS operating conditions v_{in}, i_{out}, ΔT and d every h PWM periods and estimates the current ripple and power loss through the dynamical PWA inductance model[48] and power loss model (45), combined with the converter equations (8) and (9), by applying the iterative procedure described in Section 6.1. The electrical transient is completely neglected by the algorithm, which allows only estimating the current ripple and power loss at electrical steady state. Therefore, this estimator cannot be exploited for online SMPS control. Yet, the observer performs well during the slow thermal transients.

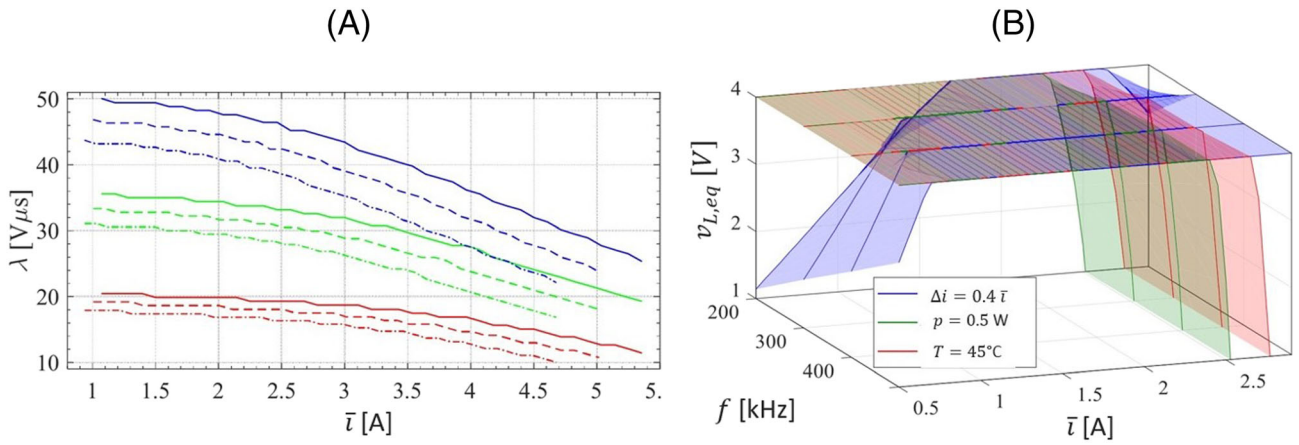

FIGURE 18 (A) boundary of real operating areas for one inductor; each color corresponds to a different value of the current ripple (increasing from blue to red), whereas each line style to a different core temperature (solid: 25°C; dashed: 50°C; dashed-dotted: 75°C). (B) boundary of constrained operating area for one inductor; the blue, green, and red surfaces correspond to assigned values of the current ripple, power loss, and temperature, respectively [Colour figure can be viewed at wileyonlinelibrary.com]

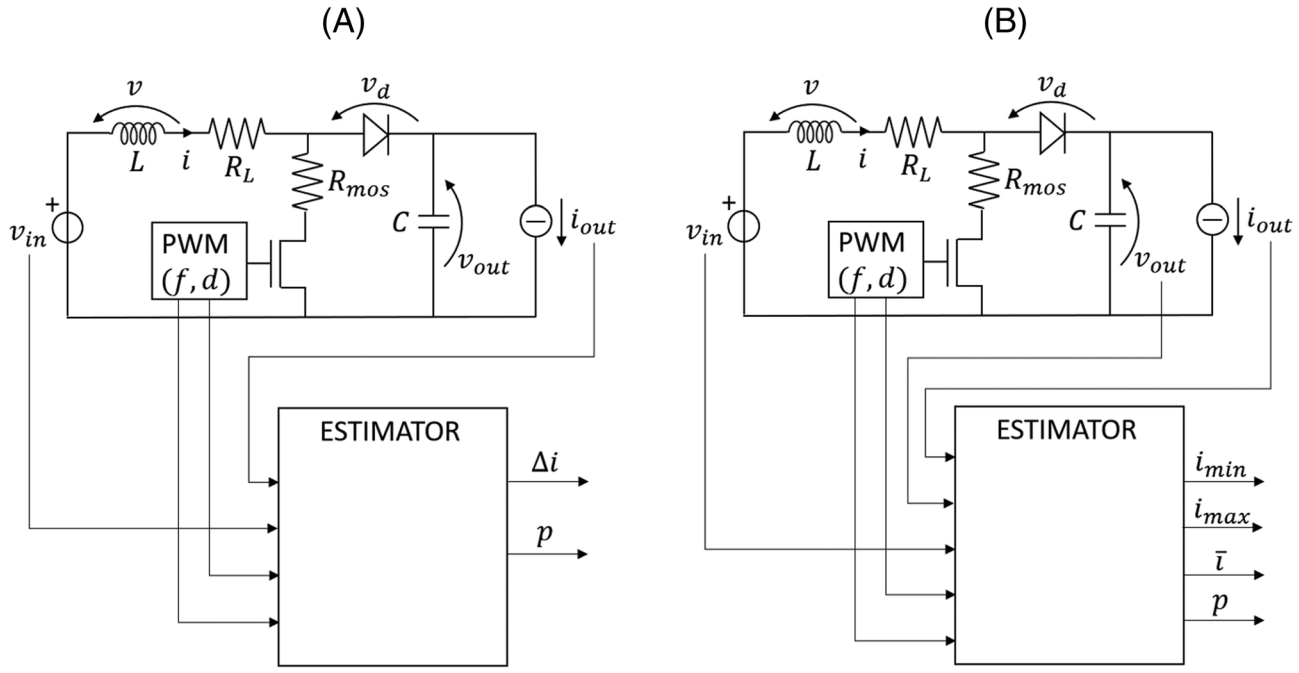

FIGURE 19 Inputs and outputs of the estimators proposed by Lodi et al,[48,86] in panels (A) and (B), respectively

An improved version of the observer[86] can estimate *analytically* the minimum, maximum, and mean inductor current and the mean power loss within a PWM period, by simulating the whole SMPS, without resorting to an iterative procedure. Different from the former observer, a term η is also estimated, based on the measurements $\hat{v}_{out}$ of the SMPS output voltage, which allows partially compensating for model parameters' uncertainties. The observer is applied to a boost converter, whose state equations (9) are modified as

$$\begin{cases} \dfrac{di}{dt} = \dfrac{v_{in,k} - (R_L + R_{mos})i + \eta}{L} \\ \dfrac{dv_{out}}{dt} = \dfrac{-i_{out,k}}{C} \end{cases} \text{for } t \in \mathcal{T}_k^{ON}, \quad \begin{cases} \dfrac{di}{dt} = \dfrac{v_{in,k} - R_L i - v_d - v_{out} + \eta}{L} \\ \dfrac{dv_{out}}{dt} = \dfrac{i - i_{out,k}}{C} \end{cases} \text{for } t \in \mathcal{T}_k^{OFF}, \tag{53}$$

where η is the solution of the following dynamical system, with null initial condition,

$$\frac{d\eta}{dt} = K(\hat{v}_{out} - v_{out}), \tag{54}$$

being K a tuning parameter. Owing to this term, the observer proves to be robust to uncertainties on the inductor series resistance R_L. This estimator exploits the dynamical PWA inductance model[44] and power loss model (46), combined with the converter equations. Unlike the previous observer, this estimator is able, in principle, to reproduce the whole current waveform during both fast electrical and slow thermal transients, provided that sufficiently fast hardware is exploited. The implementation on a high-end microcontroller or an FPGA would allow successfully combining this observer to a controller, for example, peak current mode control (see Section 6.4) or model predictive control.

6.4 | SMPS control

The hysteretic control is a simple yet effective control technique for SMPSs, widely exploited in industrial applications. Its action can be easily explained by referring to the buck and boost converters shown in Figure 7. When the output voltage exceeds an upper threshold $v_{out,\,H}$ the switch is closed, bringing the SMPS to the ON state (see Figure 20A). Vice versa, when the output voltage goes below a lower threshold $v_{out,\,L} < v_{out,\,H}$, the switch is opened (OFF state). This allows maintaining the output voltage around a reference value $v_{out,\,ref} \in (v_{out,\,L}, v_{out,\,H})$, with a ripple whose amplitude is determined by the two chosen thresholds. If the delay determined by the hysteretic comparator and the switch were zero, the voltage ripple would be exactly $v_{out,\,H} - v_{out,\,L}$. In the practice, a small delay t_d is always present, leading to an extra ripple on both the output voltage and the inductor current. These extra ripples, inversely proportional to the inductance, increase if the inductor operates in partial saturation.[17] However, the hysteretic controller dampens this effect by automatically increasing the switching frequency, leading to a constant-ripple and variable-frequency operation. This results in a marginal impact of the inductor saturation on the ripple.

Peak current mode control (PCMC) is another popular control technique adopted in SMPSs.[87] The controller operates at a constant frequency, meaning that the switch is closed (ON phase) every ΔT seconds. The OFF phase starts when the inductor current reaches a control signal i_C (see Figure 20B), depending on the difference between the desired and measured output voltage. The control signal can be constant during a PWM period, or a decreasing ramp can be subtracted to it (to implement the so-called slope compensation). In the normal steady-state operation, the duty cycle remains constant (period-1 mode); however, undesired period 2 (the duty cycle switches among two values) or even chaotic solutions could arise, if the controller parameters are not properly set. PCMC can be safely exploited also with saturating inductors,[19] as it only requires comparing the measured inductor current with a reference value. However, the common tuning rules for the controllers are valid only if the inductor works in the linear region.[88] A condition for

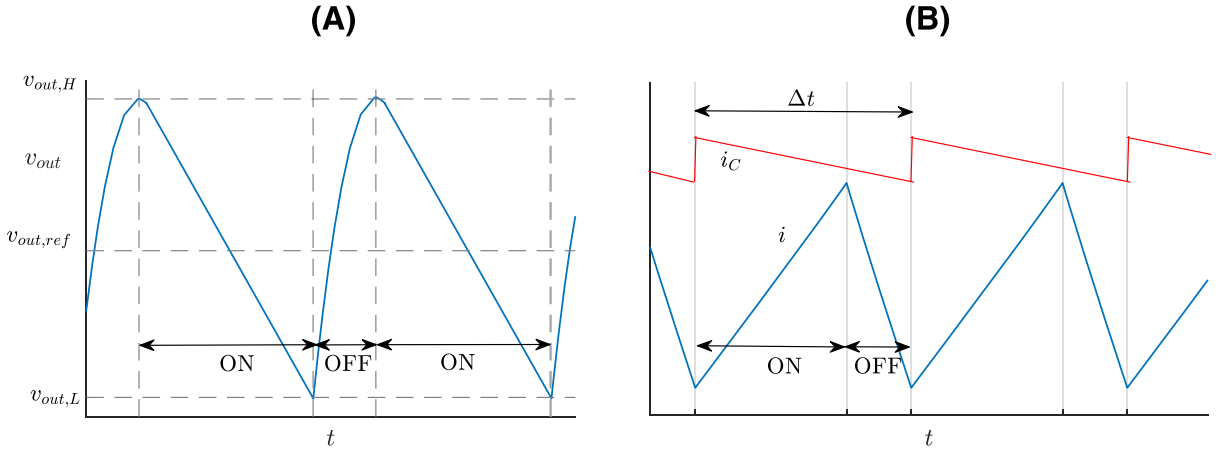

FIGURE 20 Working principle of the hysteretic control (A) and peak current mode control (B) [Colour figure can be viewed at wileyonlinelibrary.com]

period-1 operation has been proposed[19] for SMPSs with saturating inductors, which sets a lower limit for the inductance in correspondence of the peak inductor current. This inductance value can be determined by resorting to one of the inductance models described in Section 4. The use of saturable inductors in SMPSs is, therefore, a viable solution also with PCMC.

Bizzarri et al[76] show that saturating inductors can be exploited also with constant-on-time (COT) control, where the converter switch is driven by a sequence of pulses of constant width.

Mariethoz et al[45] exploit explicit model predictive control (MPC)[89] for the voltage regulation of a buck converter with a saturating inductor. The inductance is simply represented as a piecewise-constant function of the current, that is,

$$L(i) = \begin{cases} L_{nom}, \text{ if } i \le i_{sat}, \\ L_{sat}, \text{ if } i > i_{sat}, \end{cases} \tag{55}$$

being i_{sat} a current threshold to be identified. Hence, the boost converter can be modeled as a PWA system, suitable for the design of explicit MPC.[90] In short, a constrained optimization problem based on a prediction of the future evolution of the converter state is solved for a set of initial conditions, and the resulting control function (the duty cycle d) is a PWA function of the system state (i and v_{out}). MPC is a quite popular technique for the regulation of power converters;[91] however, the work by Mariethoz et al. can be considered as the first attempt to apply this control technique to a converter with a saturating inductor. The exploitation of a more accurate inductor model is a necessary step to achieve better control performances, even if this would strongly affect the computation complexity of the controller.

Özkan et al[33] apply a classical current control technique to a voltage-source converter (VSC) containing a saturating inductor. An inverse dynamical model-based compensation strategy is proposed, where the nonlinearity of the inductor due to core saturation is compensated by an inverse model, to obtain a fictitious linear inductor. A linear proportional-integral controller is then applied to the VSC. The inductance is represented as a function of the current through a third-order polynomial (see Section 4).

In other works[92-95] a second winding is wound around the inductor coil, and a current is applied to move the operating point on the $\phi - i$ characteristic to a different point, farther from the saturation region. An auxiliary control circuit is added to the conventional current controller, that determines the biasing current for the second winding. This biasing technique allows exploiting smaller inductors operating in their linear region, at the cost of an additional winding and control circuitry, increasing the overall power loss. Moreover, it is not always possible to apply a second winding to commercial inductors.

Mastromauro et al[36] apply classical resonant and repetitive current controllers to a grid converter for a photovoltaic system, with a filtering saturating inductor which connects the converter to the grid. Both PWA and polynomial models are exploited and it is shown that the harmonic compensation provided by the resonant and the repetitive controllers also mitigates the effects of the inductance saturation.

7 | CONCLUSIONS

Traditionally, inductors are modeled as linear components, where the magnetic flux is proportional to the current flowing through the windings. However, it is now evident that this represents a limitation, as also witnessed, for example, by works on pinched hysteresis loops in nonlinear inductors.[96] Tens of behavioral nonlinear models have been proposed in the last decade, able to reproduce the inductance, power loss, and temperature rise of power inductors working in their saturation region. Some models are simple to identify and evaluate, but they are accurate only for a limited set of operating conditions. Other models are more general but depend on non-easy-to-measure quantities (e.g., the inductor core temperature). Some other models depend only on electrical quantities, but they are valid at fixed room temperature and for a specific power converter. By evaluating all the proposed representations, it appears that a unified model able to accurately estimate the inductance, power loss, and temperature rise of an inductor for any SMPS in several operating conditions is still missing. A research effort is therefore necessary to combine the many available results to obtain an accurate and reliable nonlinear inductor behavioral model to be exploited for SMPS simulation, design, monitoring, and control. To the best of the authors' knowledge, only a couple of model-based estimators have been realized and a preliminary model-based controller has been proposed based on a very simple inductance model

(Equation 55). However, the achievements obtained so far motivate further research activities aimed at properly exploiting saturating inductors to increase SMPS power density.

ACKNOWLEDGMENTS

The authors would like to express their sincere appreciation to Nicola Femia and Lorenzo Repetto for many useful inputs and valuable comments.

DATA AVAILABILITY STATEMENT

Data sharing is not applicable to this article as no new data were created or analyzed in this study.

ORCID

Alberto Oliveri https://orcid.org/0000-0002-2000-6851
Matteo Lodi https://orcid.org/0000-0002-0753-7017
Marco Storace https://orcid.org/0000-0003-4958-074X

REFERENCES

1. European Commission, *The European Green Deal*. 2019. https://eur-lex.europa.eu/legal-content/EN/TXT/?uri=CELEX:52019DC0640#document2
2. Cardoso DS, Fael PO, Espírito-Santo A. A review of micro and mild hybrid systems. *Energy Rep*. 2020; 6: 385–390.
3. Al-Alawi BM, Bradley TH. Review of hybrid, plug-in hybrid, and electric vehicle market modeling studies. *Renew Sust Energ Rev*. 2013; 21:190-203.
4. Buticchi G, Bozhko S, Liserre M, Wheeler P, Al-Haddad K. On-board microgrids for the more electric aircraft—technology review. *IEEE Trans Ind Electron*. 2018;66(7):5588-5599.
5. Sahoo S, Zhao X, Kyprianidis K. A review of concepts, benefits, and challenges for future electrical propulsion-based aircraft. *Aerospace*. 2020;7(4):44.
6. Aishwarya V, Gnana SK. Review of reduced-switch multilevel inverters for electric vehicle applications. *Int J Circuit Theory Appl*. 2021; 49(9):3053-3110.
7. Reddy KJ, Natarajan S. Energy sources and multi-input DC-DC converters used in hybrid electric vehicle applications—a review. *Int J Hydrog Energy*. 2018;43(36):17387-17408.
8. Martinez W, Cortes C, Yamamoto M, Imaoka J, Umetani K. Total volume evaluation of high-power density non-isolated DC–DC converters with integrated magnetics for electric vehicles. *IET Power Electron*. 2017;10(14):2010-2020.
9. Chen J, Wang C, Chen J. Investigation on the selection of electric power system architecture for future more electric aircraft. *IEEE Trans Transp Electrification*. 2018;4(2):563-576.
10. Zaidi B, Videt A, Idir N. Optimization method of CM inductor volume taking into account the magnetic core saturation issues. *IEEE Trans Power Electron*. 2018;34(5):4279-4291.
11. Park B, Huh S, Kim J, et al. The magnetic energy harvester with improved power density using saturable magnetizing inductance model for maintenance applications near high voltage power line. *IEEE Access*. 2021;9:82661-82674.
12. Martinez W, Kimura S, Imaoka J, Yamamoto M, Cortes CA. Volume comparison of DC-DC converters for electric vehicles. In: proceedings of the IEEE Workshop on Power Electronics and Power Quality Applications (PEPQA), June 2-4, 2015. Bogota (Colombia); 1–6.
13. Parodi M, Storace M. *Linear and nonlinear circuits: Basic & advanced concepts*. Vol. 2. Springer; 2020.
14. Milner L, Rincón-Mora GA. Small saturating inductors for more compact switching power supplies. *IEEJ Trans Electr*. 2012;7(1):69-73.
15. Di Capua G, Femia N. A novel method to predict the real operation of ferrite inductors with moderate saturation in switching power supply applications. *IEEE Trans Power Electron*. 2016;31(3):2456-2464.
16. Di Capua G, Femia N, Stoyka K. Switching power supplies with ferrite inductors in sustainable saturation operation. *Int J Electr Power Energy Syst*. 2017;93:494-505.
17. Femia N, Di Capua G. Hysteretic regulators with partially-saturated inductors. In: Proceedings of the 25th IEEE International Conference on Electronics, Circuits and Systems (ICECS), December 9–12, 2018. Bordeaux (France); 417–420.
18. Di Capua G, Femia N, Stoyka K. Impact of inductors saturation on DC-DC switching regulators. In: Proceedings of the IEEE 5th International forum on Research and Technology for Society and Industry (RTSI), September 9–12, 2019. Florence (Italy); 254–259.
19. Femia N, Stoyka K, Di Capua G. Impact of inductors saturation on peak-current mode control operation. *IEEE Trans Power Electron*. 2020;35(10):10969-10981.
20. Salas R, Pleite J. Simulation of the saturation and air-gap effects in a pot ferrite core with a 2-D finite element model. *IEEE Trans Magn*. 2011;47(10):4135-4138.
21. Salas R, Pleite J. Equivalent electrical model of a ferrite core inductor excited by a square waveform including saturation and power losses for circuit simulation. *IEEE Trans Magn*. 2013;49(7):4257-4260.
22. Gurleyen H, Mese E. Analytical modeling of magnetically saturated inductance by lambert W function. *J Magn*. 2017;22(3):369-377.

23. Appino C, Khan M, De La Barriere O, Ragusa C, Fiorillo F. Alternating and rotational losses up to magnetic saturation in non-oriented steel sheets. *IEEE Trans Magn*. 2016;52(5):1-4.
24. Yahiou A, Bayadi A, Babes B. Modified method for transformer magnetizing characteristic computation and point-on-wave control switching for inrush current mitigation. *Int J Circuit Theory Appl*. 2019;47(10):1664-1679.
25. Lodi M, Oliveri A, Storace M. Behavioral models for ferrite-core inductors in switch-mode DC-DC power supplies: A survey. In: Proceedings of the 5th IEEE International forum on Research and Technology for Society and Industry (RTSI), September 9–12, 2019. Florence (Italy); 242–247.
26. Kaiser J, Duerbaum TA. An overview of saturable inductors: applications to power supplies. *IEEE Trans Power Electron*. 2021;36(9): 10766-10775.
27. TDK-Electronics, Magnetic Design Tool, Hysteresis loop of the N27 ferrite material. https://tools.tdk-electronics.tdk.com/mdt/index.php/hysteresis
28. TDK Electronics, Ferrites and accessories - processing notes. https://www.tdk-electronics.tdk.com/download/531538/67fa2f237fae90fab6f31f4a10f42772/pdf-processingnotes.pdf
29. Kool Mμ, Material curves. https://www.mag-inc.com/Products/Powder-Cores/Kool-Mu-Cores/Kool-Mu-Material-Curves
30. Coilcraft Inc., How current and power relates to losses and temperature rise. https://www.coilcraft.com/getmedia/1d7479a0-a2ce-4aae-a0a1-4d29711f7cea/doc1055_losses_temp_rise.pdf
31. Vitale G, Lullo G, Scire D. Thermal stability of a DC/DC converter with inductor in partial saturation. *IEEE Trans Ind Electron*. 2021; 68(9):7985-7995.
32. Scirè D, Vitale G, Ventimiglia M, Lullo G. Non-linear inductors characterization in real operating conditions for power density optimization in SMPS. *Energies*. 2021;14(13):3924.
33. Özkan Z, Hava AM. Current control of single-phase vsc systems with inductor saturation using inverse dynamic model-based compensation. *IEEE Trans Ind Electron*. 2019;66(12):9268-9277.
34. Lullo G, Scirè D, Vitale G. Non-linear inductor modelling for a DC/DC buck converter. *Renew Energy Power Qual J*. 2017;15:686-693.
35. Scirè D, Rosato S, Lullo G, Vitale G. A temperature dependent non-linear inductor model for a DC/DC boost converter. In: Proceedings of the 15th International Conference on Synthesis, Modeling, Analysis and Simulation Methods and Applications to Circuit Design (SMACD), July 2–5, 2018. Prague (Czech Republic); 237–239.
36. Mastromauro RA, Liserre M, Dell'Aquila A. Study of the effects of inductor nonlinear behavior on the performance of current controllers for single-phase PV grid converters. *IEEE Trans Ind Electron*. 2008;55(5):2043-2052.
37. Di Capua G, Femia N, Stoyka K, Lodi M, Oliveri A, Storace M. Ferrite inductor models for switch-mode power supplies analysis and design. In: Proceedings of the 14th International Conference on Synthesis, Modeling, Analysis and Simulation Methods and Applications to Circuit Design (SMACD), June 12–15, 2017. Giardini Naxos (Italy); 1–4.
38. Burrascano P, Di Capua G, Laureti S, Ricci M. Neural models of ferrite inductors non-linear behavior. In: Proceedings of the IEEE International Symposium on Circuits and Systems (ISCAS), May 26–29, 2019;. Sapporo (Japan); 1–5.
39. Oliveri A, Lodi M, Storace M. Accurate modeling of inductors working in nonlinear region in switch-mode power supplies with different load currents. In: proceedings of the 15th International Conference on Synthesis, Modeling, Analysis and Simulation Methods and Applications to Circuit Design (SMACD), July 2–5, 2018. Prague (Czech Republic); 233–236.
40. Oliveri A, Di Capua G, Stoyka K, Lodi M, Storace M, Femia N. A power-loss-dependent inductance model for ferrite-core power inductors in switch-mode power supplies. *IEEE Trans Circuits Syst I Regul Pap*. 2019;66(6):2394-2402.
41. Stoyka K, Di Capua G, Femia N. Modeling of stepped air-gap ferrite inductors in switching power supplies. In: Proceedings of the 25th IEEE International Conference on Electronics, Circuits and Systems (ICECS), December 9–12, 2018. Bordeaux (France); 401–404.
42. Burrascano P, Di Capua G, Femia N, Laureti S, Ricci M. Pulse compression for ferrite inductors modeling in moderate saturation. In: 2018 15th International Conference on Synthesis, Modeling, Analysis and Simulation Methods and Applications to Circuit Design (SMACD), July 2–5, 2018. Prague (Czech Republic); 229–232.
43. Burrascano P, Laureti S, Ricci M. Pulse compression modeling for voltage driven ferrite inductors in moderate saturation. In: Proceedings of the 26th IEEE International Conference on Electronics, Circuits and Systems (ICECS), November 27–29, 2019. Genova (Italy); 855–858.
44. Oliveri A, Lodi M, Storace M. A piecewise-affine inductance model for inductors working in nonlinear region. In: Proceedings of the 16th International Conference on Synthesis, Modeling, Analysis and Simulation Methods and Applications to Circuit Design (SMACD), July 15–18, 2019. Lausanne (Switzerland); 1–4.
45. Mariethoz S, Herceg M, Kvasnica M. Model predictive control of buck DC-DC converter with nonlinear inductor. In: Proceedings of the 11th Workshop on Control and Modeling for Power Electronics, August 17–20, 2008. Zurich (Switzerland); 1–8.
46. Bizzarri F, Lodi M, Oliveri A, Brambilla A, Storace M. A nonlinear inductance model able to reproduce thermal transient in SMPS simulations. In: Proceedings of the IEEE International Symposium on Circuits and Systems (ISCAS), May 26–29, 2019. Sapporo (Japan).
47. Lodi M, Bizzarri F, Linaro D, Oliveri A, Brambilla A, Storace M. A nonlinear behavioral ferrite-core inductance model able to reproduce thermal transients in switch-mode power supplies. *IEEE Trans Circuits Syst I Regul Pap*. 2020;67(4):1255-1263.
48. Lodi M, Oliveri A, Storace M. A low-cost online estimator for switch-mode power supplies with saturating ferrite-core inductors. In: Proceedings of the 26th IEEE International Conference on Electronics, Circuits and Systems (ICECS), November 27–29, 2019. Genova (Italy); 851–854.

49. Stoyka K, Di Capua G, Femia N. Normalized inductance modeling for ferrite power inductor families. In: Proceedings of the 26th IEEE International Conference on Electronics, Circuits and Systems (ICECS), November 27–29, 2019. Genova (Italy); 843–846.
50. Lodi M, Oliveri A, Storace M. Pareto-optimal selection of saturating inductors in the design of Switch-Mode Power Supplies. In: Proceedings of the 21st European Conference on Power Electronics and Applications (EPE'19 ECCE Europe), September 3–5, 2019. Genova (Italy); P–1.
51. Wolfle W, Hurley W, Arnold S. Power factor correction for AC-DC converters with cost effective inductive filtering. In: Proceedings of the 31st Annual Power Electronics Specialists Conference; June 23, 2000; Galway (Ireland): 332–337.
52. Stenglein E, Albach M. Analytical calculation method for the non-linear characteristic of ferrite-cored inductors with stepped air gap. *Electr Eng*. 2017;99(1):421-429.
53. Wens M, Thone J. MADMIX: The standard for measuring SMPS inductors. *Bodo's Power Syst*. 2015;52-54.
54. Brambilla A, Maffezzoni P. Envelope following method for the transient analysis of electrical circuits. *IEEE Trans Circuits Syst I Fundam Theory Appl*. 2000;47(7):999-1008.
55. Gheorghe AG, Constantinescu F, Marin M, Niţescu M. The envelope following analysis of a buck converter with closed loop control. In: Proceedings of the 4th International Symposium on Electrical and Electronics Engineering (ISEEE), October 11-13, 2013. Galati (Romania); 1-5.
56. Farhan M, Gad E, Nakhla M, Achar R. High order envelope following method for parallel simulation of power converter circuits. In: Proceedings of the 23rd Conference on Electrical Performance of Electronic Packaging and Systems (EPEPS), October 26–29, 2014. Portland (USA); 77–80.
57. Di Capua G, Femia N, Stoyka K. Differential evolution algorithm-based identification of ferrite core inductors saturation curves. In: Proceedings of the IEEE 13th International Conference on Industrial Informatics (INDIN), July 22–24, 2015. Cambridge (UK), 1636–1641.
58. Lodi M, Oliveri A, Storace M. Effects of parameter variation on the accuracy of a nonlinear inductor model for switch-mode power supplies applications. In: Proceedings of the IEEE International Symposium on Circuits and Systems (ISCAS), October 10–21, 2020. Seville (Spain); 1–5.
59. Coilcraft Inc., Determining inductor power losses. https://www.coilcraft.com/getmedia/236a5602-fc7f-432a-9bdb-30fd09b63837/doc486_inductorlosses.pdf
60. Würth Elektronik, Accurate inductor loss determination using Würth Elektronik's REDEXPERT. https://www.we-online.com/web/en/index.php/show/media/07_electronic_components/download_center_1/application_notes_berichte/exakte_bestimmung_von_spulenverlusten/Accurate_Inductor_Loss.pdf
61. Stoyka K, Femia N, Di Capua G. Power inductors behavioral modeling revisited. *IEEE Trans Circuits Syst I Regul Pap*. 2020;67(12):5636-5649.
62. Roshen WA. A practical, accurate and very general core loss model for nonsinusoidal waveforms. *IEEE Trans Power Electron*. 2007;22(1):30-40.
63. Stoyka K, Di Capua G, Femia N. A novel AC power loss model for ferrite power inductors. *IEEE Trans Power Electron*. 2018;34(3):2680-2692.
64. Coilcraft Inc., Current and Temperature Ratings. https://www.coilcraft.com/getmedia/42878a08-a05a-4640-9c6d-f2eb5152046c/Doc361_Current_Temp.pdf
65. Reatti A, Kazimierczuk MK. Comparison of various methods for calculating the AC resistance of inductors. *IEEE Trans Magn*. 2002;38(3):1512-1518.
66. Krings A, Soulard J. Overview and comparison of iron loss models for electrical machines. *J Electr Eng*. 2010;10(3):162-169.
67. Barg S, Ammous K, Mejbri H, Ammous A. An improved empirical formulation for magnetic core losses estimation under nonsinusoidal induction. *IEEE Trans Power Electron*. 2016;32(3):2146-2154.
68. Stenglein E, Dürbaum T. Core loss model for arbitrary excitations with DC bias covering a wide frequency range. *IEEE Trans Magn*. 2021;57(6):6302110.
69. Mayergoyz I. Hysteresis models from the mathematical and control theory points of view. *J Appl Phys*. 1985;57(8):3803-3805.
70. Jiles DC, Atherton DL. Theory of ferromagnetic hysteresis. *J Appl Phys*. 1984;55(6):2115-2120.
71. Steinmetz CP. On the law of hysteresis. *Proc IEEE*. 1984;72(2):197-221.
72. Pulse Electronics, P1172 Datasheet. https://eu.mouser.com/datasheet/2/336/-349775.pdf
73. TDK Electronics, Magnetic Design Tool. https://tools.tdk-electronics.tdk.com/mdt/index.php/
74. Van den Bossche A, Valchev VC, Georgiev GB. Measurement and loss model of ferrites with non-sinusoidal waveforms. In: Proceedings of the IEEE 35th Annual Power Electronics Specialists Conference, June 20–25, 2004. Aachen (Germany). 4814–4818.
75. Bizzarri F, Brambilla A. PAN and MPanSuite: simulation vehicles towards the analysis and design of heterogeneous mixed electrical systems. In: Proceedings of the 1st New Generation of Circuits & Systems Conference (NGCAS), September 6–9, 2017. Genova (Italy); 1-4.
76. Bizzarri F, Brambilla A, Codecasa L, Callegari S. On the benefit of adopting saturable inductors in switching-mode power-supplies: A case study. In: Proceedings of the IEEE International Symposium on Circuits and Systems (ISCAS), May 27–30, 2018. Florence (Italy); 1–5.
77. Bizzarri F, Brambilla A, El Aroudi A. Nonlinear analysis of a DC-DC boost converter working as a maximum power point tracker using analog-mixed-signal circuit simulation. In: Proceedings of the IEEE International Symposium on Circuits and Systems (ISCAS), May 26–29, 2019. Sapporo (Japan); 1–5.

78. Di Capua G, Femia N, Stoyka K. Power magnetics volume and weight reduction in aerospace power supply units. In: Proceedings of the IEEE 17th Workshop on Control and Modeling for Power Electronics (COMPEL), June 27–30, 2016. Trondheim (Norway); 1–6.
79. Di Capua G, Femia N, Stoyka K. A generalized numerical method for ferrite inductors analysis in high current ripple operation. *Integration*. 2017;58:473-484.
80. Ragusa C, Solimene L, Musumeci S, et al. Computation of current waveform in ferrite power inductors for application in buck-type converters. *J Magn Magn*. 2020;502:166458.
81. Musumeci S, Solimene L, Ragusa C, Palma M, de la Barriere O. Saturable Inductor Modelling in GaN FETs Based Synchronous Buck Converter. In: Proceedings of the International Symposium on Power Electronics, Electrical Drives, Automation and Motion (SPEEDAM), June 24-26, 2020. Sorrento (Italy); 396–401.
82. Solimene L, Musumeci S, Ragusa C. Saturable ferrite inductor parameters obtained through a double step optimization. In: Proceedings of the 55th International Universities Power Engineering Conference (UPEC), September 1–4, 2020. Turin (Italy); 1–6.
83. Ziegler S, Woodward RC, Iu HHC, Borle LJ. Current sensing techniques: A review. *IEEE Sens J*. 2009;9(4):354-376.
84. Aiello O, Fiori F. A new mirroring circuit for power MOS current sensing highly immune to EMI. *Sensors*. 2013;13(2):1856-1871.
85. Min R, Tong Q, Zhang Q, Chen C, Zou X, Lv D. Corrective frequency compensation for parasitics in boost power converter with sensorless current mode control. *Int J Electr Power Energy Syst*. 2018;96:274-281.
86. Lodi M, Oliveri A. Online estimation of the current ripple on a saturating ferrite-core inductor in a boost converter. *Sensors*. 2020; 20(10):2921.
87. Zhou G, Xu J, Wang J. Constant-frequency peak-ripple-based control of buck converter in CCM: review, unification, and duality. *IEEE Trans Ind Electron*. 2013;61(3):1280-1291.
88. Fang CC, Redl R. Subharmonic instability limits for the peak-current-controlled boost, buck–boost, flyback, and SEPIC converters with closed voltage feedback loop. *IEEE Trans Power Electron*. 2016;32(5):4048-4055.
89. Bemporad A, Morari M, Dua V, Pistikopoulos EN. The explicit linear quadratic regulator for constrained systems. *Automatica*. 2002; 38(1):3-20.
90. Bemporad A, Borrelli F, Morari M. Piecewise linear optimal controllers for hybrid systems. In: proceedings of the 2000 American Control Conference (ACC), June 28–30, 2000. Chicago, IL (USA); 1190–1194.
91. Kouro S, Cortés P, Vargas R, Ammann U, Rodriguez J. Model predictive control—a simple and powerful method to control power converters. *IEEE Trans Ind Electron*. 2008;56(6):1826-1838.
92. Beraki MW, Trovão JPF, Perdigão MS, Dubois MR. Variable inductor based bidirectional DC–DC converter for electric vehicles. *IEEE Trans Veh Technol*. 2017;66(10):8764-8772.
93. Ahsanuzzaman S, McRae T, Peretz MM, Prodić A. Low-volume buck converter with adaptive inductor core biasing. In: Proceedings of the 27th Annual IEEE Applied Power Electronics Conference and Exposition (APEC), February 5–9, 2012. Orlando, FL (USA); 335–339.
94. Hwu K, Hsiao C, Shieh JJ. Inductor saturation detection with anti-saturation control strategy applied. In: Proceedings of the IEEE 10th International Conference on Power Electronics and Drive Systems (PEDS), April 22–25, 2013. Kitakyushu (Japan); 266–270.
95. Soon JL, Raman GP, Peng JCH, Lu DDC. Current ripple reduction using AC core biasing in DC-DC converters. *IEEE Trans Ind Electron*. 2020;68(10):10058-10067.
96. Fouda ME, Elwakil AS, Radwan AG. Pinched hysteresis with inverse-memristor frequency characteristics in some nonlinear circuit elements. *Microelectron J*. 2015;46(9):834-838.
97. Reinert J, Brockmeyer A, De Doncker RW. Calculation of losses in ferro- and ferrimagnetic materials based on the modified Steinmetz equation. *IEEE Trans Ind Appl*. 2001;37(4):1055-1061.
98. Li J, Abdallah T, Sullivan CR. Improved calculation of core loss with nonsinusoidal waveforms. In: Conference Record of the 2001 IEEE Industry Applications Conference. 36th IAS Annual Meeting, September 30 – October 4, 2001. Chicago (USA); 2203–2210.
99. Venkatachalam K, Sullivan CR, Abdallah T, Tacca H. Accurate prediction of ferrite core loss with nonsinusoidal waveforms using only Steinmetz parameters. In: Proceedings of the IEEE Workshop on Computers in Power Electronics, June 3–4, 2002. Mayaguez (USA); 36–41.
100. Muhlethaler J, Biela J, Kolar JW, Ecklebe A. Core losses under the DC bias condition based on Steinmetz parameters. *IEEE Trans Power Electron*. 2011;27(2):953-963.
101. Shen W, Wang F, Boroyevich D, Tipton CW. Loss characterization and calculation of nanocrystalline cores for high-frequency magnetics applications. *IEEE Trans Power Electron*. 2008;23(1):475-484.
102. Sullivan CR, Harris JH, Herbert E. Core loss predictions for general PWM waveforms from a simplified set of measured data. In: Proceedings of the 25th Annual IEEE Applied Power Electronics Conference and Exposition (APEC), February 21–25, 2010. Palm Springs (USA); 1048–1055.
103. Sokalski K, Szczyglowski J, Najgebauer M, Wilczynski W. Losses scaling in soft magnetic materials. *COMPEL: International Journal for Computation and Maths. in Electrical and Electronic Eng.* 2007;26(3):640-649.
104. Kosai H, Turgut Z, Scofield J. Experimental investigation of DC-bias related core losses in a boost inductor. *IEEE Trans Magn*. 2013; 49(7):4168-4171.

How to cite this article: Oliveri A, Lodi M, Storace M. Nonlinear models of power inductors: A survey. *Int J Circ Theor Appl*. 2021;1-33. doi:10.1002/cta.3147

APPENDIX A: VARIANTS OF THE STEINMETZ EQUATION

In this appendix, the most relevant variants of the Steinmetz equation are summarized. Some of the used parameters are defined in Section 5.1.

A.1 | Models for unbiased inputs

Reinert et al[97] propose a modified Steinmetz equation (MSE), valid also for unbiased non-sinusoidal fields. The core loss is expressed as

$$p_{core,v} = \left(k f_{eq}^{\alpha-1} B_{pk}^{\beta}\right) f, \text{ with } f_{eq} = \frac{2}{\left(\pi B_{pk}\right)^2} \int_0^{\Delta T} \left(\frac{dB}{dt}\right)^2 dt. \tag{A1}$$

The expression of the equivalent frequency f_{eq} is derived from the mean time derivative of the field B within a magnetization period.[97]

Li et al[98] describe some anomalies in the MSE and propose a generalized Steinmetz equation (GSE), where

$$p_{core,v} = \frac{1}{\Delta T} \int_0^{\Delta T} k_1 \left|\frac{dB}{dt}\right|^{\alpha} |B(t)|^{\beta-\alpha} dt, \tag{A2}$$

which reduces to the classical Steinmetz equation in the case of sinusoidal field, for an appropriate value of coefficient k_1.

An improved generalized Steinmetz equation (IGSE) is proposed by Venkatachalam et al,[99] which has better accuracy than GSE and allows taking into account waveforms with multiple peaks, that is, minor and major hysteresis cycles. Basically, the term $B(t)$ in Equation (A2) is replaced by B_{pk}. Other variants have been proposed,[100-103] but the IGSE is considered as the best method in terms of accuracy and from a practical point of view.[67]

Some models are available, which are specific for square-wave voltages, a typical situation in SMPSs. Van den Bossche et al[74] and Barg et al[67] express explicitly the power loss of a ferrite core in case of a square-wave voltage with duty cycle d as

$$p_{core,v} = k(2f)^{\alpha} B_{pk}^{\beta} \left[d^{1-\alpha} + (1-d)^{1-\alpha}\right] \text{ Van den Bossche etal.} \tag{A3}$$

$$p_{core,v} = \frac{\pi}{4} k 2^{-\alpha} f^{\alpha} B_{pk}^{\beta} \left[d^{1-\alpha} + (1-d)^{1-\alpha}\right] \text{ Barg etal.} \tag{A4}$$

A.2 | Models for biased inputs

The following formulations include a dependence of the core loss on the bias field B_{dc} or H_{dc}.

The MSE[97] can be further modified in order to take into account the effect of B_{dc}. In particular, the coefficient k in Equation (A1) can be rewritten as

$$k = k'\left(1 + c_1 B_{dc} e^{-B_{pk}/c_2}\right), \tag{A5}$$

being k', c_1 and c_2 fitting parameters. Muhlethaler et al[100] express parameters k, k_1 and β of the SSE or IGSE as fourth-order polynomials of H_{dc}.

Kosai et al[104] include the presence of bias and saturation as follows,

$$p_{core,v} = \frac{k}{e^a} f^{\alpha} B_{pk}^{\beta} e^{a(\mu/\mu_{dc})^{\gamma}}, \tag{A6}$$

where μ and μ_{dc} are the permeability computed at $B = 0$ and $B = B_{dc}$, respectively, and a and γ are fitting parameters.

A loss model valid for arbitrary excitation signals with one maximum and one minimum was recently proposed by Stenglein et al,[68] where

$$p_{core,v} = E_{v,hyst}(B_{pk}, B_{dc})\left[1 + c\left(\frac{1}{B_{pk}}\int_0^T \left|\frac{d^2B}{dt^2}\right| dt\right)^{\gamma}\right] f, \tag{A7}$$

being c a fitting parameter. The term $E_{v,\,hyst}(B_{pk}, B_{dc})$ is the quasi-static energy loss measured at steady-state for different values of B_{pk} and B_{dc}. A polynomial interpolation can be utilized to determine $E_{v,\,hyst}$ for given values of B_{pk} and B_{dc}. Parameters c and γ are frequency-independent and can be obtained by applying only one waveform $B(t)$. The core loss data for sinusoidal excitation of $B(t)$ without dc bias, as usually provided by core manufacturers, suffice for the extraction of c and γ.